Variability of Lidar-Derived Particle Properties Over West Africa Due to Changes in Absorption: Towards an Understanding

Igor Veselovskii[1], Qiaoyun Hu[2], Philippe Goloub[2], Thierry Podvin[2], Mikhael Korenskiy[1], Yevgeny Derimian[2], Michel Legrand[2], Patricia Castellanos[3]

[1]*General Physics Institute, Moscow, Russia.*
[2]*Univ. Lille, CNRS, UMR 8518 - LOA - Laboratoire d'Optique Atmospherique, Lille F-59000, France*
[3]*NASA Goddard Space Flight Center, Greenbelt, USA*

Abstract

Measurements performed in Western Africa (Senegal) during the SHADOW-2 field campaign are analyzed to show that spectral dependence of the imaginary part of the complex refractive index (CRI) of dust can be revealed by lidar-measured particle parameters. Observations in April 2015 provide good opportunity for such study, because, due to high optical depth of the dust, exceeding 0.5, the extinction coefficient could be derived from lidar measurements with high accuracy and contribution of other aerosol types, such as biomass burning, was negligible. For instance, in the second half of April 2015, AERONET observations demonstrated a temporal decrease of the imaginary part of CRI at 440 nm from approximately 0.0045 to 0.0025. This decrease is in line with a change in the relationship between the lidar ratios (the extinction-to-backscattering ratio) at 355 nm and 532 nm (S_{355} and S_{532}). For instance in the first half of April, S_{355}/S_{532} is as high as 1.5 and the backscatter Angstrom exponent A_β, is as low as -0.75, while after 15 April S_{355}/S_{532}=1.0 and A_β is close to zero. The aerosol depolarization ratio δ_{532} for the whole April exceeded 30% in the height range considered, implying that no other aerosol, except dust, occurred. The performed modeling confirmed that the observed S_{355}/S_{532} and A_β values match the spectrally dependent imaginary part of the refractive index as can be expected for mineral dust containing iron oxides. The second phase of the SHADOW-2 campaign was focused on evaluation of the lidar ratio of smoke and estimates of its dependence on relative humidity (RH). For five studied smoke episodes the lidar ratio increases from 44±5 sr to 66±7 sr at 532 nm and from 62±6 sr to 80±8 sr at 355 nm, when RH varied from 25% to 85%. Performed numerical simulations demonstrate, that observed ratio S_{355}/S_{532}, exceeding 1.0 in the smoke plumes, can indicate to increase of the imaginary part of the smoke particles in the ultraviolet (UV).

1. Introduction

Atmospheric dust provides significant impacts on the Earth's climate system and this impact remains highly uncertain (IPCC report, 2013). In modeling the direct aerosol effect, the

vertical profile of the aerosol extinction is one of the basic input parameters, and when this profile is derived from the elastic backscatter lidar observations, the knowledge of the extinction-to-backscatter ratio (so called lidar ratio) is essential (Klett, 1985). Although the desert dust in source regions is sometimes qualified as "pure dust", it is always a mixture of various elements, e.g. iron oxides, clays, quartz and calcium–rich species, which proportions can vary (Sokolik and Toon, 1999; Wagner et al., 2012; Di Biagio et al., 2017, 2019 and references therein). Thus, the dust optical properties, and hence the lidar ratio (S) can vary, depending on the relative abundance of various minerals in emission sources. The imaginary part of the complex refractive index (CRI) of different minerals can vary spectrally and often exhibits an increase in UV spectral region for dust, containing iron oxides. Therefore, the retrieval of the dust extinction profiles from elastic backscatter lidar observation should account for the spectral variation of the lidar ratio.

Raman and HSRL lidars are capable of providing independent profiling of aerosol backscattering and extinction coefficients (Ansmann et al., 1992), and therefore are widely used to measure the lidar ratios of dust from different origins (e.g. Sakai et al., 2003; Papayannis et al., 2008, 2012; Xie et al., 2008; Ansmann et al., 2011; Mamouri et al., 2013; Burton et al., 2014; Nisantzi et al., 2015; Giannakaki et al., 2016; Hofer et al., 2017, 2019; Soupiona et al., 2018, 2019). The African deserts are the largest sources of mineral dust and numerous studies have been conducted for quantifying the particle intensive parameters (parameters independent of concentration) during dust transport from this source region to Europe and over the Atlantic Ocean (Mattis et al., 2002; Amiridis et al., 2005; Mona et al., 2006; Papayannis et al., 2008; Preißler et al., 2013; Groß et al., 2015; Rittmeister et al., 2017; Haarig et al. 2017). The dust properties are, however, modified during this transport, experiencing mixing and aging processes, thus the characterization of the dust properties near the source regions is highly important for the evaluation the parameters of "pure dust".

The lidar ratios at 355 nm and 532 nm (S_{355} and S_{532}) were measured during the SAMUM-1 and 2 experiments in Morocco and Capo Verde respectively (Esselborn et al., 2009; Tesche et al., 2009, 2011; Groß et al., 2011; Ansmann et al., 2011), as well as during the more recent SHADOW-2 experiment in Senegal (Veselovskii et al., 2016, 2018). The lidar ratios S_{355} and S_{532} measured during SAMUM experiments did not present significant spectral dependence. For example, for SAMUM-2 campaign, the averaged values of S_{355} and S_{532} were 53±10 sr and 54±10 sr respectively (Tesche et al., 2011). During SHADOW, however, S_{355} significantly exceeded S_{532} in many dust episodes, which was linked to an increase of the imaginary part of CRI of dust at 355 nm (Veselovskii et al., 2016).

The dust backscattering coefficient, in contrast to the extinction coefficient, is sensitive to the imaginary part of CRI (Perrone et al., 2004; Veselovskii et al., 2010; Gasteiger et al., 2011). Recall, that the particle extinction is the sum of absorption and scattering, and increase of absorption is accompanied by decrease of scattering, leading to weak dependence of the extinction on the imaginary part (Veselovskii et al. 2010, Fig.6). Thus, it is expected that enhanced absorption in the UV should increase the lidar ratio. In turn, the ratio S_{355}/S_{532} should characterize the spectral variation of the imaginary part of CRI. The latest version of AERONET products (3.0) provides inversions of the lidar related properties, including the lidar ratio, from almucantar scans with ground-based sun photometers. For these products, the shortest available wavelength is 440 nm. Despite the imaginary part at 440 nm (Im_{440}) is lower than Im_{355}, AERONET observations still show an increase of absorption at 440 nm in respect to 675 nm that yields a ratio of S_{440}/S_{675} close to 1.4 for Saharan dust (Shin et al., 2018). The goal of this work is to analyze the correlation of variations of Im_{440} from AERONET with measured values from lidar to reveal the effect of dust absorption on lidar-derived aerosol properties. We focus on height and day-to-day variations of the dust intensive properties, such as S_{355} and S_{532}, depolarization ratio (δ), as well as the extinction and backscatter Ångström exponents (A_α and A_β respectively) measured during several strong dust episodes in April 2015 during the SHADOW-2 campaign.

The smoke aerosol particles, typically originated from biomass burning, can also have a pronounced spectral dependence of absorption (Nicolae et al., 2013). This is generally due to presence of carbonaceous particles with organic compounds, so-called brown carbon (BrC) (Sun et al., 2007; Kirchstetter, et al., 2004). The Sahel region is known for seasonal biomass burning caused by human activity on combustion of agricultural waste that can produce an abundant amount of BrC. The smoke can also be mixed with mineral dust during long-range transport or in the emission origin (Haywood et al., 2008). During the SHADOW-2 the observation period included the biomass burning season, thus an additional effort was dedicated to the examination of the spectral lidar ratio variability of transported biomass burning aerosol under different environmental conditions and presents a supplementary subject of the current study.

The paper is organized as follows. Section 2 describes the lidar system and provides the main expressions used for the data analysis. Several strong dust episodes, in April 2015, are analyzed in Section 3. In Section 4, the smoke episodes occurring from December 2015 to January 2016, are used to evaluate the variation of the smoke lidar ratio with relative humidity. The paper is finalized with conclusion.

2. Experimental setup and data analysis

The observations were performed with LILAS multiwavelength Raman lidar during SHADOW-2 campaign at Mbour, Senegal. Information related to the SHADOW-2 and observation site is presented in Veselovskii et al. (2016). The LILAS is based on a tripled Nd:YAG laser with a 20 Hz repetition rate and pulse energy of 90/100/100 mJ at 355/532/1064 nm. The aperture of the receiving telescope is 400 mm. During the campaign, LILAS configuration (3β+2α+1δ) allowed the measurement of three particle backscattering (β_{355}, β_{532}, β_{1064}), two extinction coefficients (α_{355}, α_{532}) and depolarization ratio at 532 nm (δ_{532}). To improve the performance of the system at 532 nm the rotational Raman channel was used instead of the vibrational one (Veselovskii et al, 2015). The measurements were performed at a 47 degrees angle to horizon. The backscattering coefficients and depolarization ratios were calculated with a 7.5 m range resolution (corresponding to 5.5 m vertical resolution), while the range resolution of extinction coefficient varied from 50 m (at 1000 m) to 125 m (at 7000 m). Particle extinction and backscattering coefficients at 355 nm and 532 nm are calculated from elastic and Raman backscatter signals, as described in Ansmann et al. (1992) and corresponding uncertainties are shown on the plots. An additional Raman reception channel at 408 nm was setup for profiling the water vapor mixing ratio (WVMR) (Whiteman et al., 1992).

The particle depolarization ratio δ, determined as a ratio of cross- and co-polarized components of the particle backscattering coefficient, was calculated and calibrated the same way as described in Freudenthaler et al. (2009). The relative uncertainty of depolarization measurements due to calibration is estimated as ±10%. To analyze the complex aerosol mixtures, containing dust (d) and smoke (s), we can write $\beta = \beta^d + \beta^s$ and $\alpha = \alpha^d + \alpha^s$. The depolarization ratio of such a mixture is therefore:

$$\delta = \frac{\left(\frac{\delta^d}{1+\delta^d}\right)\beta^d + \left(\frac{\delta^s}{1+\delta^s}\right)\beta^s}{\frac{\beta^d}{1+\delta^d} + \frac{\beta^s}{1+\delta^s}} \quad (1)$$

Here δ^d and δ^s are the particle depolarization ratios of dust and smoke components respectively.

To characterize the spectral dependence of the extinction (α) and backscattering (β) coefficients, the corresponding Ångström exponents are introduced as:

$$A_\alpha = \frac{\ln\left(\frac{\alpha_{\lambda_1}}{\alpha_{\lambda_2}}\right)}{\ln\left(\frac{\lambda_2}{\lambda_1}\right)} \text{ and } A_\beta = \frac{\ln\left(\frac{\beta_{\lambda_1}}{\beta_{\lambda_2}}\right)}{\ln\left(\frac{\lambda_2}{\lambda_1}\right)} \quad (2)$$

Where α_{λ_1}, α_{λ_2}, β_{λ_1}, β_{λ_2} are the extinction and backscattering coefficients at wavelengths λ_1 and λ_2. For the mixture of smoke and dust, the extinction Ångström exponent (EAE) can be calculated from the ratio $\frac{\alpha_{\lambda_1}}{\alpha_{\lambda_2}}$:

$$\frac{\alpha_{\lambda_1}}{\alpha_{\lambda_2}} = \frac{\alpha^d_{\lambda_1} + \alpha^s_{\lambda_1}}{\alpha^d_{\lambda_2} + \alpha^s_{\lambda_2}} = \frac{\alpha^d_{\lambda_1}}{\alpha^d_{\lambda_2}} \frac{\left(1 + \frac{\alpha^s_{\lambda_1}}{\alpha^d_{\lambda_1}}\right)}{\left(1 + \frac{\alpha^s_{\lambda_2}}{\alpha^d_{\lambda_2}}\right)} = \frac{\alpha^d_{\lambda_1}}{\alpha^d_{\lambda_2}} \frac{\left(1 + \frac{\alpha^s_{\lambda_2}(\frac{\lambda_2}{\lambda_1})^{A^s_\alpha}}{\alpha^d_{\lambda_2}(\frac{\lambda_2}{\lambda_1})^{A^d_\alpha}}\right)}{\left(1 + \frac{\alpha^s_{\lambda_2}}{\alpha^d_{\lambda_2}}\right)} = \frac{\alpha^d_{\lambda_1}}{\alpha^d_{\lambda_2}} \frac{\left(1 + \frac{\alpha^s_2}{\alpha^d_{\lambda_2}}\left(\frac{\lambda_2}{\lambda_1}\right)^{(A^s_\alpha - A^d_\alpha)}\right)}{\left(1 + \frac{\alpha^s_{\lambda_2}}{\alpha^d_{\lambda_2}}\right)} \quad (3)$$

Here A^d_α and A^s_α are the Ångström exponents of dust and smoke. The Ångström exponent of the mixture is obtained from (3):

$$A_\alpha = \frac{\ln\frac{\alpha_{\lambda_1}}{\alpha_{\lambda_2}}}{\ln\frac{\lambda_2}{\lambda_1}} = A^d_\alpha + \frac{1}{\ln\frac{\lambda_2}{\lambda_1}} \ln\left[\frac{\left(1 + \frac{\alpha^s_{\lambda_2}}{\alpha^d_{\lambda_2}}\left(\frac{\lambda_2}{\lambda_1}\right)^{(A^s_\alpha - A^d_\alpha)}\right)}{\left(1 + \frac{\alpha^s_{\lambda_2}}{\alpha^d_{\lambda_2}}\right)}\right] \quad (4)$$

The backscattering Ångström exponent (BAE) can be calculated in a similar way. And finally, the lidar ratio of the aerosol mixture is calculated as:

$$S = \frac{S^d\beta^d + S^s\beta^s}{\beta^d + \beta^s} = S^d + \frac{\beta^s}{\beta}(S^s - S^d) \quad (5)$$

where S^d and S^s are the lidar ratios of dust and smoke.

3. Dust observations in March and April 2015

The aerosol over West Africa presents strong seasonal variations. The spring is characterized by strong dust emission, while, during winter season, intense forest fires occurring in the equatorial regions emit smoke particles that are transported over Senegal (Veselovskii et al., 2018). The SHADOW-2 campaign included the following periods of measurements: 13 March – 25 April 2015, 8–25 December 2015 and 5-24 January 2016, so numerous dust and smoke episodes were observed. In our analysis of lidar-derived aerosol properties, we considered also aerosol columnar properties provided by AERONET (Holben et al. 1998) and aerosol profiles predicted by the Modern-Era Retrospective analysis for Research and Applications, Version 2 (MERRA-2) aerosol reanalysis (Gelaro et al., 2017; Randles et al., 2017). MERRA-2 is the first long-term global reanalysis to assimilate space-based aerosol observations and include

their radiative coupling with atmospheric dynamics. MERRA-2 is driven by the Goddard Earth Observing System (GEOS) model version 5 that includes the Goddard Chemistry, Aerosol, Radiation and Transport (GOCART) module. GOCART models the sources, sinks, and transformation of the following five aerosol species as external mixtures: dust, organic carbon (OC), black carbon (BC), sulfates (SU) and sea salt (SS). Dust and sea salt are represented by five non-interacting size bins, and have wind-speed dependent emissions. The MERRA-2 reanalysis assimilates AOD observations from the twin Moderate Resolution Imaging Spectroradiometer (MODIS) instruments, MODIS-Terra and MODIS-Aqua, as well as the AERONET ground-based sun photometer network. In addition, the profiles of meteorological variables (P, T, RH), provided by radio-sondes at the Dakar airport, located ~70 km from the M'bour site, were also available. The relative humidity (RH) profiles over the M'bour site were calculated from the combination of lidar-derived WVMR and temperature profile from radiosounding.

Fig.1 shows the aerosol optical depth at 532 nm (AOD_{532}) for March, April and December 2015 recalculated from AERONET AOD at 500 nm using the 440-675 nm Ångström exponent. The same figure shows the AODs for the five aerosol species used in MERRA-2 model, such as dust, organic carbon (OC), black carbon (BC), sulfates (SU) and sea salt (SS). The optical depths provided by MERRA-2 and AERONET are in a good agreement. Dust is the predominant aerosol component for all three months with the highest values of AOD in April. The contribution of organic carbon (the main component of the biomass burning products) is significant in December, when the forest fire season starts in equatorial regions, though noticeable amount of OC is predicted also for March and for the beginning of April. The contribution of BC and SU to the total AOD is low: the sum of the corresponding AODs is below 0.1 for all three months.

The single scattering albedo (SSA) over the M'Bour site in 2015 provided by AERONET at 440 and 675 nm is shown in Fig.2. The SSA_{675} is above 0.97 for March – April period, but at 440 nm dust absorption is stronger and, in March, SSA_{440} is about 0.9. However, in the middle of April, SSA_{440} increases up to 0.95, indicating that aerosols become less absorbing at shorter wavelengths. We can thus expect that variation of SSA at 355 nm between April and March should be even stronger. In our study we consider two groups of observations. The first group corresponds to the beginning of April, when SSA at 440 nm was lower. The second group covers the second half of April, when SSA at 440 nm increased. By analyzing these two groups we expect to reveal the effect of aerosol absorption, on lidar-derived aerosol properties.

3.1. Dust episode on 1 – 4 April 2015

In the beginning of April the dust was transported by Continental trades (Harmattan) from the northeastern/eastern drylands. For period 1 - 4 April, as follows from Fig.1b, the AOD_{532} over Dakar increased up to 1.0. Fig.3 shows the spatio-temporal distributions of the aerosol backscattering coefficient β_{532}, particle depolarization ratio δ_{532}, and water vapor mixing ratio for the nights 1-2, 2-3 and 3-4 April 2015. The corresponding airmass back-trajectories, shown in Fig.4, demonstrate that, on 1-2 and 2-3 April, air masses at all heights arrive from the North-East, whereas on 3-4 April the air masses above 2500 m are advected from the East. These air masses are characterized by higher humidity and may contain biomass-burning products. During these three nights, the linear particle depolarization ratio and WVMR present some evolution. On 1-2 April δ_{532} exceeds 30% and does not change significantly within the dust layer, even if some decrease is observed above 2000 m after 03:00 UTC. By 3-4 April the depolarization ratio above 2500 m decreases below 25%, simultaneously with increase of the WVMR. During the dust episode, the relative humidity did not exceed 20% on 1-3 April, but on 3-4 April it increased up to 40% above 2500 m.

Vertical profiles of dust particle properties such as aerosol extinction coefficients α_{355}, α_{532}, particle depolarization ratio δ_{532} and lidar ratios S_{355}, S_{532} are shown on Fig.5 for the three observation periods on 1, 2-3 and 3-4 April 2015. The profiles of backscattering coefficients for 2-3 and 3-4 April are given by Fig.6, while the extinction and backscatter Ångström exponents, calculated at 355 and 532 nm wavelengths for three temporal intervals from Fig.5, are presented in Fig.7. During all three observation periods A_α is slightly negative (A_α = -0.1±0.1) up to 2000 m. For the dust component, MERRA-2 provides value of A_α=-0.14, which agrees with observations. Above 2000 m, A_α exhibits some increase, which is most significant on 3-4 April, when A_α reaches 0.3±0.1 at 4000 m height. Simultaneous decrease of δ_{532} indicates to the possible presence of smoke particles above 2000 m. The backscatter Ångström exponent A_β, in contrast with A_α, is sensitive to the spectral dependence of the imaginary part of CRI, thus yielding complicated vertical variability of A_β. In particular, on 2-3 April A_β decreases from -0.5 to -0.7 within 1500–2500 m height range, when A_α remains stable.

As follows from Fig.5, on 1 April the lidar ratio S_{355}=70±6 sr does not change with height, while S_{532} gradually decreases from 60±5 sr at 1000 m to 50±4 sr at 3000 m height. On sessions that followed (Fig.5b,c) the lidar ratios at both 355 nm and 532 nm decreased. Thus, the range of lidar ratios variation for the dust episode on 1-4 April is 60-70 sr at 355 nm and 45-60 sr at 532 nm. The lidar ratios (S_{355} and S_{532}) modeled by MERRA-2 for the dust component are also shown on Fig. 5. The corresponding lidar ratio values are of 70 sr and 42 sr respectively and do not vary with altitude as the model optical properties of all dust size bins based on spectral

complex refractive indices from the Optical Properties of Aerosols and Clouds (OPAC) tables (Hess et al. 1998) and the spheroidal shape models developed by Meng et al. (2010) are the same and fixed, as dust is treated as hydrophobic. Modeled value S_{355} is near the top of the range of observed values, while modeled S_{532} underestimates the observations.

The gradual decrease of S_{532} with height in Fig.5a,c is however unusual. There are, at least, two possible reasons to explain S_{532} height variation. The first one can be the presence of non-dust particles, for example, smoke. The second reason is that the properties (composition) of dust change with height. If non-dust particles are present, the particle intensive properties, such as S, δ and A_α should vary with height in consistent way. The MERRA-2 modeling reported in Fig.1 shows that in the beginning of April the organic carbon is the second main contributor to the AOD, after dust. We should recall, however, that the model can provide a realistic range of OC variation, however not necessarily reproducing the exact spatio-temporal distribution of OC extinction coefficient.

In the dust episode considered, the most significant smoke contribution was observed on 3-4 April. Fig.8a shows the profiles of measured α_{355} and α_{532} together with MERRA-2 modeled extinction coefficients at 532 nm for five aerosol components. The extinction Ångström exponents measured by lidar and modeled by MERRA-2 for dust component are given by Fig.8b. The same figure shows also the lidar derived water vapor mixing ratio profile together with the relative humidity. At low altitudes (below 2500 m), where aerosol is represented by pure dust, the measured and modeled values of extinction coefficients are close. Above 2500 m the measured value of α_{355} exceeds that of α_{532}, indicating the presence of smoke particles, while modeled contribution of OC to the total extinction is very low. The measured extinction Ångström exponent is about -0.1 below 2000 m, which well agrees with modeling results for pure dust. Increase of WVMR and RH above 2000 m coincides with growth of the A_α. For the considered case, the model reproduces correctly the dust loading, but underestimates the smoke contribution. At 3500 m, the difference between measured and modeled α_{532} is about 0.045 km^{-1} which can be attributed to the smoke contribution.

Dust and smoke particles contributions to the total backscattering coefficient can be also separated on the basis of the depolarization measurements, assuming that depolarization ratios of these particles are known (Tesche et al., 2009). The results of such decomposition are presented in Fig.8c, assuming 35% and 7% for dust and smoke depolarization ratio. The δ_{532}=7% was the lowest value that we observed in elevated smoke layers during the SHADOW experiment (Veselovskii et al., 2018), however, due to large difference of smoke and dust depolarization ratios, the choice of exact value for the smoke did not influence significantly the results. The

contribution of smoke to the total β_{532} at 3500 m is 0.0009 $km^{-1}sr^{-1}$. For the smoke lidar ratio of 50 sr at 532 nm (validity of this choice will be discussed in section 3.3), the smoke extinction coefficient is about 0.045 km^{-1}. This value agrees well with smoke contribution obtained from Fig.8a at 3500 m and thus can be used for estimating the smoke effect on the intensive aerosols properties derived from lidar measurements.

The depolarization ratio of the "dust-smoke" mixture, calculated with expression (1), matches the observed value since decomposition in Fig.8c is based on depolarization measurements. The Ångström exponent at 3500 m computed with (4) for α_{532}^{s} =0.045 km^{-1}, α_{532}^{d} =0.147 km^{-1}, A_{α}^{d} =-0.1 and A_{α}^{s} =0.9 yields $A_{\alpha} = 0.28$, which is close to observed value 0.26±0.08. Hence, the observed variation of A_{α} above 2000 m on 3-4 April is well explained by smoke contribution. In a similar way, using (5) we can estimate the smoke lidar ratio (S_{532}^{s}) that would match the observed decrease of S_{532}. To explain decrease of the lidar ratio at 3500 m from 50 sr to 45 sr, the smoke lidar ratio should be about 25 sr, which is unrealistically small (Burton et al., 2012). Such small lidar ratio could be attributed to the maritime aerosol, but then the lidar ratios at both wavelengths should decrease simultaneously. Recall that on 1-2 April smoke contribution was significantly lower, while decrease of S_{532} is about 10 sr. Thus, smoke particles presence cannot explain the observed decrease of S_{532} and it should be probably attributed to changes of dust composition (and so the imaginary part) with height.

Smoke lidar ratio is usually assumed to be higher than that of dust (Tesche et al., 2011; Burton et all., 2012), meanwhile in Fig 5c the lidar ratio S_{532} is not increased in presence of the smoke particles. It should however be noticed that our results were obtained at low RH. The smoke particles are hygroscopic and the lidar ratio should increase with RH. The way to characterize S_{532}^{s} over Dakar site can be based on the analysis of the lidar measurements during smoke episodes within height range where smoke contribution becomes predominant. The results of such analysis will be discussed later in section 3.3.

3.2. Dust episodes on 14 and 24 April 2015.

In the second part of April 2015, dust AOD_{532} exceeded 1.0 (Fig.1b) and contributions of other aerosol components were insignificant. Meanwhile, as follows from Fig.2, SSA_{440} increased after 15 April, thus dust became less absorbing in the UV, which should influence the lidar-derived aerosol intensive properties. Fig.9 shows the values of the extinction coefficients and lidar ratios at 355 nm and 532 nm, together with depolarization ratio δ_{532} and the Ångström exponents A_{α} and A_{β} observed on 14 April (00:00 – 05:00 UTC) and 23-24 April (23:00-06:00

UTC). The first case is a "transition day" when SSA_{440} starts to increase. The aerosol extinction profiles presented in Fig.9a show that two dust layers can be distinguished. In the first layer (below 2.5 km), aerosol intensive properties are similar to that of 1-4 April with $S_{355}>S_{532}$, slightly negative A_α = -0.1 and A_β as low as -0.35. In the second layer S_{355} and S_{532} coincide and both A_α and A_β are close to zero. The depolarization ratio in the second layer is about 31%, slightly lower than in the first one. Thus, we can assume that increase of the imaginary part in UV in the first layer is more significant, than in the second one. From the analysis of airmass back-trajectories given in Fig.10, we can conclude that the air masses in the first layer originate from the Northeastern/Eastern drylands, while in the second layer the air masses arrive from the East. After 14 April, S_{355} and S_{532} coincided for the whole height range and results obtained on 23-24 April (Fig.8 c, d) are the example of such observations. Airmass back-trajectories show that the air masses at both 2.0 and 3.0 km height are transported from East. The ratio S_{355}/S_{532} is close to 1.0 within the whole dust layer and both Ångström exponents A_α, A_β are close to zero. Thus, the results from Figs.9, 10 are indicating that lidar-derived aerosol properties depend on the dust source origin.

3.3 Analysis of lidar ratio variations in March – April 2015

Fig.11 summarizes the lidar ratio measurements for period from 29 March to 24 April 2015 (first phase of SHADOW ended on 25 April). Here we focus on the properties of "pure dust", thus do not show results before 29 March, when AOD was lower and the contribution of other aerosol types could be significant (Fig.1). For the Fig.11 we have chosen height intervals, where S value is stable and δ exceeds 30%. For example, on 14 and 24 April lidar ratios are averaged inside 2.7-3.7 km and 2.0-4.0 km layers respectively. For the period considered, S_{355} and S_{532} vary in the ranges 50 sr – 80 sr and 45 sr - 60 sr respectively with a mean values of 62 sr and 51 sr. Enhanced variability of S_{355} compared to S_{532} can be explained by variation of the imaginary part at 355 nm. At the beginning of the 29 March and 8 April dust episodes, S_{355}/S_{532} ratio is as high as 1.5 and then gradually decreases. After 14 April, S_{355}/S_{532} ratio becomes close to 1.0, thus S presents no spectral dependence.

The day-to-day variation of the aerosol column properties, including the spectrally dependent complex refractive index, can be obtained from AERONET (Holben et al., 1998). Fig.12 shows the imaginary part of the aerosol refractive index at 440 nm and 675 nm (Im_{440}, Im_{675}) provided by AERONET for the same period of time as in Fig.11. The Im_{440} strongly decreases after 14 April, correlating with the decrease of S_{355}/S_{532} ratio in Fig.11, which corroborates the suggestion, that variations of S_{355}/S_{532} ratio are related to variation of dust

absorption in the UV. The retrieved real part (Re) of the complex refractive index oscillates around Re=1.45 and shows no significant spectral dependence. Correlation between enhancement of Im_{440}, with in respect to Im_{675}, and increase of lidar-derived S_{355}/S_{532} is clearly seen in Fig.13, showing time – series of difference Im_{440}-Im_{675} and S_{355}/S_{532} ratio.

To analyze the variations of the observed lidar ratios and the Ångström exponents, a simplified numerical simulation has been performed. For a realistic modeling of the dust lidar ratio, various mixtures of different mineral components and particles shapes should be considered. Sensitivity of the modeling results to the dust mixture parameters was demonstrated in study of Gasteiger et al. (2011). Such detailed modeling, however, is out of the scope of the present paper. Here we only intend to evaluate the main impact when the imaginary part of CRI is modified.

The lidar ratio depends not only on the complex refractive index but also on the dust particle size distribution (PSD). The PSDs provided by AERONET on 2 and 23 April 2015 (three distributions for each day) are shown in Fig.14. The PSDs are similar and the effective radii for both days are about 0.75 μm, thus, difference in S observed for 2 and 23 April should be related mainly to the complex refractive index. Fig.15a presents modeled S_{355} and S_{532} lidar ratios together with the extinction and backscattering Ångström exponents A_α, A_β as a function of the imaginary part. Computations were performed for the AERONET derived size distribution on 23 April from Fig.14 using the assembly of randomly oriented spheroids (Dubovik et al., 2006) with the real part Re=1.55. S_{355} and S_{532} increase with the imaginary part and the ratio S_{355}/S_{532} is about 1.1. Extinction coefficient is slightly sensitive to the imaginary part, thus increase of S in Fig.15 is due to decrease of backscattering coefficient with Im. The modeled A_α is about A_α=0.1, while A_β decreases with Im to A_β=-0.2. To estimate the influence of a spectrally dependent imaginary part Im(λ) on A_β, we have also performed computations assuming a fixed Im_{532}=0.002 and only Im_{355} is free to vary. Corresponding results are shown in Fig.15a with open stars. Spectral dependence of the imaginary part significantly decreases A_β: for Im_{355}=0.005 (Im_{355} – Im_{532}=0.003), A_β decreases to -0.75.

We should recall however, that for the second half of April the observed ratio S_{355}/S_{532}, was about 1.0, and both extinction and backscatter Ångström exponents were close to zero. To figure out the kind of PSD that would reproduce those observations, we retrieved the PSD from 3β+2α measurements, as described in Veselovskii et al. (2002, 2010). For that purpose, data from 23-24 April (Fig.9), averaged within 2-3 km layer, were inverted and corresponding PSD is shown in Fig.14 with red line. Inversion was performed for the assembly of randomly oriented spheroids, in assumption of spectrally independent refractive index. Due to the limited number of

input data (five) we are able to reproduce only the main features of the PSD. The maximum of this lidar derived PSD is shifted towards larger radii, with respect to the AERONET size distribution, but at the same time, retrieved PSD contains significant contribution from the fine particles. The simulation results for this lidar derived PSD, are given by Fig.15b. The lidar ratios S_{355}, S_{532} for all values of the imaginary part are close. The backscatter and extinction Ångström exponents are close to zero, matching the observations of the second half of April 2015. Thus simulation results demonstrate dependence on the PSD chosen, but in both cases these lead to the same conclusion: observed low values of A_β can not be reproduced without accounting for spectral dependence of the imaginary part.

To compare computations and observations, information upon Im_{355} and Im_{532} values is needed. The recently measured refractive indices of dust, sampled at different regions of Africa, are presented by Di Biagio et al. (2019). In particular, for the countries located North and East of Senegal, the aerosol imaginary parts at 370, 470, 520, 660 nm are of 0.0043, 0.0033, 0.0026, 0.0013 for Mauritania and 0.0048, 0.0038, 0.0030, 0.0024 for Mali respectively. The highest values of lidar ratios, observed in our measurements, are about 60 sr and 80 sr at 532 nm and 355 nm respectively. Corresponding imaginary parts of CRI from Fig.15 can be estimated as Im_{532}=0.002-0.003 and Im_{355}=0.005-0.006, which agrees with results presented by Di Biagio et al. (2019). Assuming Im_{355}=0.005 and Im_{532}=0.002, the modeled ratio S_{355}/S_{532} is about 1.44 and A_β is about -0.75 for both AERONET and lidar derived PSDs, which again reasonably agrees with observations. The modeling performed is very simplified, still it confirms that the observed values of S_{355}/S_{532} ratio and A_β can be explained by the spectral dependence of the imaginary part of CRI.

Thus, based on our measurement results, two types of dust can be distinguished. The first type has high S_{355}/S_{532} ratio (up to 1.5). Such kind of dust is characterized by an increase of the imaginary part in the UV and it was observed, for example, during 29 March and 10 April episodes. For the second type, the ratio $S_{355}/S_{532}\approx1.0$, so variation of the imaginary part of the refractive index between 532 and 355 nm wavelengths should be smaller than for the first type. Such dust was observed in the second half of April 2015. Both types are characterized by high depolarization ratio, δ_{532} values, exceeding 30%, so depolarization measurements at 532 nm are not capable to discriminate between these two types of dust.

The difference in the observed dust properties is probably related to the mineralogical characteristics in the source region. From the back-trajectories analysis presented in Figs. 4 and 10 one can suppose that the first type of dust was transported from the North–East, while the second type from the East. In order to verify if a difference in the dust emission source region and transport take place, we also analyzed the Infrared Difference Dust Index (IDDI) derived

from the Meteosat Second Generation (MSG) geostationary satellite imagery in the thermal infrared (TIR). The IDDI is developed by Legrand et al. (1985, 2001) originally for the Meteosat First Generation (MFG) and is based on impact of the airborne mineral dust on the TIR radiation emitted by the terrestrial surface. The physical principle of the IDDI derivation is in thermal contrast between terrestrial surface and atmosphere and the best sensitivity is found at around noon time when the surface temperature is maximal (Legrand et al., 1988). The IDDI product shows that brightness temperature of terrestrial surface observed by satellite can be reduced up to about 50°K in presence of airborne mineral dust, while reduction by about 10°K already indicates a major dust event (Legrand et al., 2001). A direct relationship between the IDDI and aerosol optical thickness in solar spectrum and visibility was also found (Legrand et al., 2001). It should be mentioned here that the IDDI was initially developed for MFG and the absolute consistence with the IDDI values from MSG should be examined due to differences in spatial and spectral resolutions between two sensors. However, the physical principles used for the IDDI determination are the same and a direct application of the MFG IDDI algorithm to MSG was found as possible. Moreover, tests showed that the absolute values of IDDI for a coincident overlapping period of MFG and MSG are very close. Nevertheless, employment of the IDDI from MSG is indeed applicable for the required in the current analysis purpose of solely dust spatial patterns detection.

The IDDI calculations, applied to the MSG images taken during the field campaign, clearly show a major dust event in northern and central Africa. The elevated IDDI values over Senegal are also visible. The IDDI images show distinguishable changes in the emission sources and transport features during the different phases of the observations. For instance, Fig. 16 shows that the dust emissions during the first phase of the event are originated in south Algeria, Mauritania and Mali (examples of images from 29 and 30 March 2015). Weeks later, spatial patterns of the elevated IDDI are shifted to south and show source regions in south of Niger (Fig.15c, d). Of course, attribution of emission sources mineralogy to aerosol spectral absorption is a complex task (Alfaro., et al 2004; Lafon et al., 2006; Di Biagio et al., 2017, 2019) and it is difficult to point to a specific source that could clearly explain the observed in this study change in the aerosol absorbing properties. However, the IDDI images clearly suggest a change in the dust transport regime that is consistent with the change in the dust optical properties.

4. Smoke episodes in December 2015 – January 2016

During the SHADOW campaign, we had several strong smoke episodes in December 2015 – January 2016, when air mass transported the products of biomass burning from the areas of intensive forest fires in equatorial region. The relative humidity in the advected smoke layers

varied from episode to episode, allowing evaluation of the RH influence on the smoke lidar ratios S_{355}, S_{532}. We should keep in mind, however, that for different days the smoke particles could have different chemical composition, so evaluated RH dependence can be considered as semi-quantitative only. The spatio-temporal evolution of the particle backscattering coefficient and depolarization ratio at 532 nm, during the 14-15 December 2015 smoke episode, is given in Fig.17. The same figure shows also the water vapor mixing ratio, a convenient tracer to identify wet air mass arrived from the equatorial region. The smoke particles are usually contained in elevated layers, being mixed with dust (Veselovskii et al., 2018). The height ranges where the smoke particles are predominant can be identified by low depolarization ratio and enhanced WVMR. For event considered, the smoke particles are predominant above 1500 m after midnight.

The vertical profiles of α_{355}, α_{532}, S_{355}, S_{532}, A_α, A_β together with the water vapor mixing ratio and the relative humidity, for 15 December (04:00 – 06:00 UTC), are shown in Fig.18. The same figure presents decomposition of β_{532} to the dust and smoke contributions, based on depolarization measurements (Tesche et al., 2011). The smoke episodes are characterized by different relative humidity within the elevated layer. On 15 December, RH is about 40% in the 1500 – 2100 m range and the ratio $\frac{\beta_{532}^s}{\beta_{532}}$ is about of 0.57 at 2000 m. The lidar ratio S_{532} decreases from 50 sr to 44 sr in 1000 m - 2000 m range, while S_{355} rises from 58 sr to 67 sr, thus S_{355} significantly exceeds S_{532}. We should recall that lidar ratios presented in Fig.18 are attributed to dust- smoke mixture. In principle, we can estimate S_{532}^s using Eq.5, because the ratio $\frac{\beta_{532}^s}{\beta_{532}}$ is available. Corresponding S_{532}^s profile obtained for assumed S_{532}^d =50 sr is shown in Fig.18a (black line). S_{532}^s is about 40 sr at 2000 m and it is close to measured S_{532} value. In the smoke layer, the extinction Ångström exponent A_α, can exceed A_β, due to negative contribution of A_β^d. In particular, on 15 December A_α is about 1.1, while A_β is close to zero.

To estimate the dependence of smoke lidar ratios S_{355} and S_{532} on RH, five smoke episodes on 14-15, 15-16, 22-23, 24-25 December 2015 and 19-20 January 2016 were analyzed. S_{532} and S_{355}, together with relative humidity and the $\frac{\beta_{532}^s}{\beta_{532}}$ ratio are summarized, for these episodes, in Table 1. The heights chosen correspond to the values of relative humidity close to maximum. The calculated values of RH are characterized by high uncertainties, because lidar and sonde measurements are not collocated. Estimations of the corresponding uncertainties are

460 also given by Table 1. The lidar ratio values from Table 1 are plotted in Fig.19 as a function of
461 RH. These plots, however, should be taken with care, because, due to variation of chemical
462 composition and the aging processes, results may depend not only on RH. Moreover, the dust
463 particles occurring in the elevated layers, as discussed, can introduce an additional ambiguity in
464 the results. Nevertheless, Fig.19 demonstrates a clear increasing trend of S with RH, at both
465 wavelengths. From this figure, one can also conclude that S_{355} always exceeds S_{532} and, that S_{532}
466 for smoke can be as small as 44±5 sr at low humidity. The small values of S_{532} for the "fresh
467 smoke" (about 40 sr) were reported also by Burton et al. (2012).
468 To compare our observations with the lidar ratios used in the MERRA-2 model, we have
469 also performed the simulation of $S_{532}^{OC}(RH)$ and $S_{355}^{OC}(RH)$ dependence for organic carbon (OC)
470 based on the particle parameters and hygroscopic growth factor from MERRA-2 model. In
471 MERRA-2 the organic carbon is the main component of the biomass burning products. The
472 imaginary part of the OC increases in the UV due to the presence of "brown carbon" (BrC),
473 which is a subset of organic carbon with strong absorption in the UV region (Bergstrom et al.,
474 2007; Torres et al., 2007). The majority of BrC is emitted into the atmosphere through low-
475 temperature, incomplete combustion of biomass. In the newest development of GEOS, biomass
476 burning OC is now emitted as a new BrC tracer species that uses Im_{532}=0.009 and Im_{355}=0.048
477 values (Hammer et al. 2016). Thus, the spectral behavior of the imaginary part of organic carbon
478 refractive index depends on contribution of the BrC fraction to the primary organic carbon and
479 on the physical-chemical processes in the smoke layer during its transportation. As a result, the
480 spectral dependence of Im can present strong variations. In our study, the computations at 355
481 nm were performed for four values of the imaginary part of dry particles Im_{355}=0.048, 0.03, 0.02,
482 0.01. At 532 nm two values Im_{532}=0.005 and 0.009 were considered. The parameters of the dry
483 particle size distribution, the real part of CRI and the hygroscopic growth factor used in
484 computations are given in Veselovskii et al. (2018). The particles are assumed to be
485 homogeneous spheres and an increase of the volume for every RH value (calculated from the
486 growth factor) occurs due to water uptake. Thus both the real and the imaginary part of CRI
487 depend on RH.
488 The results of the simulations, shown in Fig.19, demonstrate strong dependence of the
489 organic carbon lidar ratio on the imaginary part of dry particles and on the relative humidity. For
490 Im_{355}=0.048, for all RH, S_{355} is above 95 sr, which strongly exceeds the observed values. For
491 lower Im_{355} the S_{355} (RH) dependence is more pronounced and for Im_{355} within the range 0.01-
492 0.02, computed S_{355} are close to observed values. Computed S_{532} values at low RH exceed the

493 measured ones, but for RH>70% agreement between measurements and GEOS assumed optical
494 properties for OC becomes reasonable.
495
496 **5. Summary and conclusion**
497 Our study shows the impact of the imaginary part variation on the lidar-derived dust
498 properties. In contrast to extinction, the backscattering coefficient, and so the lidar ratio, are
499 sensitive to the imaginary part of CRI. Hence, S_{355}/S_{532} ratio can be an indicator of the imaginary
500 refractive index enhancement in the UV. Measurements performed during the SHADOW
501 campaign, in dust conditions, show a correlation between the decrease of Im_{440}, derived from
502 AERONET observations, and the decrease of lidar-derived S_{355}/S_{532} ratio. Namely, in the second
503 half of April 2015, S_{355}/S_{532} decreased from 1.5 to 1.0, when Im_{440} decreased from 0.0045 to
504 0.0025. Our numerical simulations confirm, that observed S_{355}/S_{532} (ratio close to 1.5) and A_β
505 (value close to -0.75) can be due to spectral variation of the imaginary part, attributed to iron
506 oxides contained in dust particles. The simulations were performed for the model of randomly
507 oriented spheroids, however, we should recall, that increase of the particle lidar ratio with the
508 imaginary part should occur for any particle shape.
509 Thus, April 2015 observations suggest the presence of different dust types, characterized
510 by distinct spectral dependence of $Im(\lambda)$. The analysis of backward trajectories and IDDI derived
511 from MSG geostationary satellite confirms different air mass and dust particles transport features
512 in the beginning and at the end of April. Hence, the observed variations of S_{355}/S_{532} can be
513 related to the source region mineralogy. During April, the particle depolarization systematically
514 exceeded 30%, therefore no discrimination between different types of dust was possible.
515 Dependence of S_{355}/S_{532} ratio on dust origin, in particular, could explain, why during SAMUM
516 experiments no significant spectral dependence of the lidar ratio was observed.
517 The results presented in this study demonstrate also that, for the selected temporal
518 interval, the dust lidar ratios may present significant variation with height. Dust of different size
519 and mineralogical composition can have different deposition rate, hence, complex refractive
520 index can be height-dependent. For instance, on April 1st, the S_{532} decreased with height from 60
521 sr to 50 sr within 1000–3000 m range, while depolarization ratio exceeded 30%. The analysis of
522 this episode showed that variation of the lidar ratio is entirely attributed to variations of dust
523 characteristics; the smoke aerosol contribution was insignificant. The data also demonstrate that
524 a seemingly uniform dust layer may have quite a complex height variation. The results therefore
525 suggest the relevance of including a varying mineralogy in radiative and climatic modeling of
526 desert dust impacts. Dust mineralogy should be also taken into account, when possibility of the

particle microphysical parameters characterization on a base of multiwavelength lidar measurements is analyzed (Perez-Ramirez et al., 2019, 2020).

During December – January, the dry season in western Africa, our observations allowed in addition the analysis of biomass burning aerosol properties. These particles are a product of the seasonal forest fires and intensive agricultural waste combustion and can contain a substantial amount of organic compounds, characterized by an enhanced imaginary part in UV (so called BrC). For this aerosol type, the Im(λ) dependence should increase the lidar ratio at 355 nm and influence S_{355}/S_{532}. The smoke particles can be also hydrophilic and the lidar ratio can therefore exhibit a strong dependence on RH. Several strong smoke episodes were observed during the SHADOW campaign. While we were able to evaluate the RH profiles, the dependence of the smoke lidar ratio with RH has been estimated. The results obtained should be taken as semi-qualitative only, due to possible variation of smoke particles composition from episode to episode and due to the presence of dust particles. Nevertheless, the results clearly demonstrate an increase of S_{532} from 44±5 sr to 66±7 sr and of S_{355} from 62±6 sr to 80±8 sr, when the RH increased from 25% to 85%.

We would like to conclude that the multi-wavelengths Raman and depolarization lidar measurements in western Africa enabled quite unique and comprehensive profiling of dust and smoke spectral absorption properties. The results demonstrated a high variability of the lidar ratio and the presence of its spectral dependence. Our study is one of the first attempts to track aerosol composition variability using lidar measurements and to understand the mechanism underlying the observed variations. However, the results presented were obtained for a single region in western Africa. It is important to repeat such studies at different locations around the world, including the Middle East, Central and East Asia, Australia, and North Amerika in order to improve our knowledge on real-world dust optical properties, needed in climate relevant atmospheric modelling.

Author contributions. IV processed the data, and wrote the paper. QH and TP performed the measurements. PG supervised the project and helped with paper preparation. MK developed software for data analysis. YD and ML analyzed the satellite data and PC provided MERRA-2 simulations.

Data availability. Lidar measurements are available upon request (philippe.goloub@univ-lille.fr).

Competing interests. The authors declare that they have no conflict of interest.

Acknowledgments: The authors are very grateful to **t**he CaPPA project (Chemical and Physical Properties of the Atmosphere), funded by the French National Research Agency (ANR) through the PIA (Programme d'Investissement d'Avenir) under contract "ANR-11-LABX-0005-01" and by the Regional Council“ Nord-Pas de Calais » and the "European Funds for Regional Economic Development (FEDER). We would like to acknowledge the AERONET team at NASA/Goddard Space Flight Center in Greenbelt, MD, and Service National d'Observation PHOTONS from University of Lille/CNRS/INSU operating under ACTRIS-FR research infrastructure, for providing high-quality data. Development of lidar data analysis algorithms was supported by Russian Science Foundation (project 16-17-10241).

Table 1. Lidar ratios S_{355}, S_{532} for five smoke episodes in December 2015 – January 2016 and corresponding the relative humidity RH. The table provides also the height and temporal interval of observations. The contribution of the smoke particles to the total backscattering $\frac{\beta_{532}^{s}}{\beta_{532}}$ is derived from depolarization measurements.

Date	Height, m	Time, UTC	$\frac{\beta_{532}^{s}}{\beta_{532}}$	RH, %	S_{355}, sr	S_{532}, sr
15 Dec	2000	04:00-06:00	0.57	42±8	67±7	44±5
15 Dec	1850	19:20-20:30	0.57	25±6	62±6	50±5
23 Dec	2250	05:00-07:00	0.65	65±13	76±8	56±6
24 Dec	3200	19:00-23:00	0.66	75±14	76±8	62±6
20 Jan	4500	01:00-07:00	0.8	85±15	80±8	66±7

References

Amiridis, V., Balis, D. S., Kazadzis, S., Bais, A., Giannakaki, E., Papayannis, A., and Zerefos, C.: Four-year aerosol observations with a Raman lidar at Thessaloniki, Greece, in the framework of European Aerosol Research Lidar Network (EARLINET), J. Geophys. Res., 110, D21203, doi:10.1029/2005JD006190, 2005.

Alfaro, S. C., Lafon, S., Rajot, J. L., Formenti, P., Gaudichet, A., and Maille, M.: Iron oxides and light absorption by pure desert dust: An experimental study, J. Geophys. Res., 109, D08208, doi:08210.01029/02003JD004374, 2004.

Ansmann, A., Wandinger, U., Riebesell, M., Weitkamp, C.and Michaelis,W., "Independent measurement of extinction and backscatter profiles in cirrus clouds by using a combined Raman elastic-backscatter lidar", Appl. Opt. 31, 7113–7131, 1992.

Ansmann, A., Petzold, A., Kandler, K., Tegen, I., Wendisch, M., Müller, D., Weinzierl, B., Müller, T., Heintzenberg, J.: Saharan Mineral Dust Experiments SAMUM–1 and SAMUM–2: what have we learned?, Tellus, 63B, 403–429, 2011.

Burton, S. P., Ferrare, R. A., Hostetler, C. A., Hair, J.W., Rogers, R. R., Obland, M. D., Butler, C. F., Cook, A. L., Harper, D. B., and Froyd, K. D.: Aerosol classification using airborne High Spectral Resolution Lidar measurements – methodology and examples, Atmos. Meas. Tech., 5, 73–98, doi:10.5194/amt-5-73-2012, 2012.

Burton, S. P., Vaughan, M. A., Ferrare, R. A. and Hostetler, C. A.: Separating mixtures of aerosol types in airborne High Spectral Resolution Lidar data. Atmos. Meas. Tech., 7, 419–436, 2014.

Di Biagio, C., Formenti, P., Balkanski, Y., Caponi, L., Cazaunau, M., Pangui, E., Journet, E., Nowak, S., Caquineau, S., Andreae, M. O., Kandler, K., Saeed, T., Piketh, S., Seibert, D., Williams, E., and Doussin, J.-F.: Global scale variability of the mineral dust long-wave refractive index: a new dataset of in situ measurements for climate modeling and remote sensing, Atmos. Chem. Phys., 17, 1901-1929, https://doi.org/10.5194/acp-17-1901-2017, 2017.

Di Biagio, C., Formenti, P., Balkanski, Y., Caponi, L., Cazaunau, M., Pangui, E., Journet, E., Nowak, S., Andreae, M. O., Kandler, K., Saeed, T., Piketh, S., Seibert, D., Williams, E., and Doussin, J. – F.: Complex refractive indices and single scattering albedo of global dust aerosols in the shortwave spectrum and relationship to iron content and size, Atm. Chem. Phys., 19, 15503–15531, 2019.

Dubovik, O., Sinyuk, A., Lapyonok, T., Holben, B.N., Mishchenko, M., Yang, P., Eck, T.F., Volten, H., Munoz, O., Veihelmann, B., van der Zande, W.J., Leon, J.-F., Sorokin, M., Slutsker, I.: Application of spheroid models to account for aerosol particle nonsphericity in

remote sensing of desert dust, *J. Geophys. Res*., 111, D11208, doi:10.1029/2005JD006619, 2006.

Esselborn, M., Wirth, M., Fix, A., Weinzierl, B., Rasp, K., Tesche, M., and Petzold, A.: Spatial distribution and optical properties of Saharan dust observed by airborne high spectral resolution lidar during SAMUM 2006, Tellus B, 61, 131–143, doi:10.1111/j.1600-0889.2008.00394.x, 2009.

Freudenthaler,V., Esselborn, M.,Wiegner, M.,Heese, B., Tesche, M. and co-authors: Depolarization ratio profiling at severalwavelengths in pure Saharan dust during SAMUM 2006, *Tellus* 61B, 165–179, 2009.

Gasteiger, J., Wiegner, M., Groß, S., Freudenthaler, V., Toledano, C., Tesche, M., and Kandler, K.: Modeling lidar-relevant optical properties of complex mineral dust aerosols, Tellus B, 63, 725-741, 2011.

Gelaro, R., McCarty, W., Suarez, M.J., Todling, R., Molod, A., Takacs, L., Randles, C.A., Darmenov, A., Bosilovich, M.G., Reichle, R., Wargan, K., Coy, L., Cullather, R., Draper, C., Akella, S., Buchard, V., Conaty, A., Da Silva, A.M., Gu, W., Kim, G.K., Koster, R., Lucchesi, R., Merkova, D., Nielsen, J.E., Partyka, G., Pawson, S., Putman, W., Rienecker, M., Schubert, S.D., Sienkiewicz, M., and Zhao, B.: The Modern-Era Retrospective Analysis for Research and Applications, Version 2 (MERRA-2), Journal of Climate, 30, 5419-5454 2017.

Giannakaki, E., van Zyl, P. G., Müller, D., Balis, D., and Komppula, M.: Optical and microphysical characterization of aerosol layers over South Africa by means of multi-wavelength depolarization and Raman lidar measurements, Atmos. Chem. Phys., 16, 8109–8123, 2016.

Groß, S., Tesche, M., Freudenthaler, V., Toledano, C., Wiegner, M., Ansmann, A., Althausen, D., and Seefeldner, M.: Characterization of Saharan dust, marine aerosols and mixtures of biomassburning aerosols and dust by means of multi-wavelength depolarization and Raman lidar measurements during SAMUM 2, Tellus B, 63, 706724, doi:10.1111/j.1600-0889.2011.00556.x, 2011.

Groß, S., Freudenthaler, V., Schepanski, K., Toledano, C., Schäfler, A., Ansmann, A., and Weinzierl, B.: Optical properties of long-range transported Saharan dust over Barbados as measured by dual-wavelength depolarization Raman lidar measurements, Atmos. Chem. Phys., 15, 11067–11080, https://doi.org/10.5194/acp-15-11067-2015, 2015.

Haarig, M., Ansmann, A., Althausen, D., Klepel, A., Groß, S., Freudenthaler, V., Toledano, C., Mamouri, R.-E., Farrell, D. A., Prescod, D. A., Marinou, E., Burton, S. P., Gasteiger, J., Engelmann, R., and Baars, H.: Triple-wavelength depolarization ratio profiling of Saharan

651 dust over Barbados during SALTRACE in 2013 and 2014, Atmos. Chem. Phys., 17, 10767–
652 10794, 2017.
653 Haywood, J. M., Pelon, J., Formenti, P., Bharmal, N., Brooks, M., Capes, G., Chazette, P., Chou,
654 C., Christopher, S., Coe, H., Cuesta, J., Derimian, Y., Desboeufs, K., Greed, G., Harrison,
655 M., Heese, B., Highwood, E. J., Johnson, B., Mallet, M., Marticorena, B., Marsham, J.,
656 Milton, S., Myhre, G., Osborne, S. R., Parker, D. J., Rajot, J. L., Schulz, M., Slingo, A.,
657 Tanre, D., and Tulet, P.: Overview of the Dust and Biomass-burning Experiment and African
658 Monsoon Multidisciplinary Analysis Special Observing Period-0, Journal of Geophysical
659 Research-Atmospheres, 113, 10.1029/2008jd010077, 2008.
660 Hammer, M. S., Martin, R. V., van Donkelaar, A., Buchard, V., Torres, O., Ridley, D. A., and
661 Spurr, R. J. D.: Interpreting the ultraviolet aerosol index observed with the OMI satellite
662 instrument to understand absorption by organic aerosols: implications for atmospheric
663 oxidation and direct radiative effects, Atmos. Chem. Phys., 16, 2507–2523, 2016.
664 Hess, M., Koepke, P., and Schult, I.: Optical properties of aerosols and clouds: The software
665 package OPAC, Bulletin of the American Meteorological Society, 79, 831–844, 1998.
666 Hofer, J., Althausen, D, Abdullaev, S. F., Makhmudov, A. N., Nazarov, B. I., Schettler, G.,
667 Engelmann, R., Baars, H., Fomba, K. W., Müller, K., Heinold, B., Kandler, K., and
668 Ansmann, A.: Long-term profiling of mineral dust and pollution aerosol with
669 multiwavelength polarization Raman lidar at the Central Asian site of Dushanbe, Tajikistan:
670 case studies, Atmos. Chem. Phys., 17, 14559–14577, 2017.
671 Hofer, J., Ansmann, A., Althausen, D., Engelmann, R., Baars, H., Abdullaev, S.F., and
672 Makhmudov, A.N.: Long-term profiling of aerosol light-extinction, particle mass, cloud
673 condensation nuclei, and ice-nucleating particle concentration over Dushanbe, Tajikistan, in
674 Central Asia, Atm. Chem. Phys. Disc. doi.org/10.5194/acp-2019-963.
675 Holben, B.N., Eck, T.F., Slutsker, I., Tanre, D., Buis, J.P., Setzer, A., Vermote, E., Reagan, J.A.,
676 Kaufman, Y.J., Nakajima, T., Lavenu, F., Jankowiak, I., Smirnov, A.: AERONET- A
677 federated instrument network and data archive for aerosol characterization. Remote Sensing
678 of Environment 66, 1-16, 1998.
679 IPCC: Climate Change 2013: The Physical Science Basis. Contribution of Working Group I to
680 the Fifth Assessment Report of the Intergovernmental Panel on Climate Change, edited by:
681 Stocker, T. F., Qin, D., Plattner, G.-K., Tignor, M., Allen, S. K., Boschung, J., Nauels, A.,
682 Xia, Y., Bex, V., and Midgley, P. M., Cambridge University Press, Cambridge, UK and New
683 York, NY, USA, 1535 pp., https://doi.org/10.1017/CBO9781107415324, 2013.
684 Kandler, K., Lieke, K., Benker, N., Emmel, C., Küpper, M., Müller-Ebert,D., Ebert, M.,
685 Scheuvens, D., Schladitz, A., Schütz, L., Weinbruch, S.: Electron microscopy of particles

collected at Praia, Cape Verde, during the Saharan Mineral Dust Experiment: Particle chemistry, shape, mixing state and complex refractive index. Tellus 63B, 475-496, 2011.

Kirchstetter, T. W., Novakov, T., and Hobbs, P. V.: Evidence that the spectral dependence of light absorption by aerosols is affected by organic carbon, J. Geophys. Res.-Atmos., 109, D21208, https://doi.org/10.1029/2004JD004999, 2004.

Klett J.D., "Lidar inversion with variable backscatter/extinction ratios", Appl.Opt. 24, 1638-1643, 1985.

Lafon, S., Sokolik, I. N., Rajot, J. L., Caquineau, S., & Gaudichet, A.: Characterization of iron oxides in mineral dust aerosols: Implications for light absorption. Journal of Geophysical Research, 111(D21), 2006. https://doi.org/10.1029/2005JD007016

Legrand, M., Bertrand, J. J., Desbois, M., Menenger, L., and Fouquart, Y.: The potential of infrared sattelite data for the retrieval of Saharan – dust optical depth over Africa, Journal of Applied Meteorology, 28, 309-319, 1989.

Legrand, M., Plana-Fattori, A., and N'Doume, C.: Satellite detection of dust using the IR imagery of Meteosat 1. Infrared difference dust index, Journal of Geophysical Research-Atmospheres, 106, 18251-18274, 2001.

Mamouri, R. E., Ansmann, A., Nisantzi, A., Kokkalis, P., Schwarz, A., and Hadjimitsis, D.: Low Arabian dust extinction-to- backscatter ratio, Geophys. Res. Lett., 40, 4762–4766, 2013.

Mattis, I., Ansmann, A., Müller, D., Wandinger, U., and Althausen, D.: Dual-wavelength Raman lidar observations of the extinction-to-backscatter ratio of Saharan dust, Geophys. Res. Lett., 29, 1306, doi:10.1029/2002GL014721, 2002.

Meng, Z., Yang, P., Kattawar, G. W., Bi, L., Liou, K. N., Laszlo, I.: Single-scattering properties of tri-axial ellipsoidal mineral dust aerosols: A database for application to radiative transfer calculations, J. Aerosol Science 41, 501–512, 2010.

Mona, L., Amodeo, A., Pandolfi, M., and Pappalardo, G.: Saharan dust intrusions in the Mediterranean area: three years of Raman lidar measurements, J. Geophys. Res., 111, D16203, doi:10.1029/2005JD006569, 2006.

Nicolae D., A. Nemuc, D. Müller, C. Talianu, J. Vasilescu, L. Belegante, and A. Kolgotin: Characterization of fresh and aged biomass burning events using multi-wavelength Raman lidar and mass spectrometry, J. Geophys. Res. 118, 2956–2965, doi:10.1002/jgrd.50324, 2013.

Nisantzi, A., Mamouri, R. E., Ansmann, A., Schuster, G. L., and Hadjimitsis, D. G.: Middle East versus Saharan dust extinction-to-backscatter ratios, Atmos. Chem. Phys., 15, 7071–7084, 2015.

Papayannis, A., Amiridis, V., Mona, L., Tsaknakis, G., Balis, D., Bösenberg, J., Chaikovski, A., De Tomasi, F., Grigorov, I., Mattis, I., Mitev, V., Müller, D., Nickovic, S., Pérez, C., Pietruczuk, A., Pisani, G., Ravetta, F., Rizi, V., Sicard, M., Trickl, T., Wiegner, M., Gerding, M., Mamouri, R. E., D'Amico, G., and Pappalardo, G.: Systematic lidar observations of Saharan dust over Europe in the frame of EARLINET (2000–2002), J. Geophys. Res., 113, D10204, doi:10.1029/2007JD009028, 2008.

Papayannis, A., Mamouri, R. E., Amiridis, V., Remoundaki, E., Tsaknakis, G., Kokkalis, P., Veselovskii, I., Kolgotin A., Nenes, A. and Fountoukis, C.: Optical-microphysical properties of Saharan dust aerosols and composition relationship using a multi-wavelength Raman lidar, in situ sensors and modelling: a case study analysis", Atmos. Chem. Phys. 12, 4011-4032 (2012).

Perez-Ramirez, D., Whiteman D.N., Veselovskii, I., Colarco, P., Korenski, M., da Silva, A.: Retrievals of aerosol single scattering albedo by multiwavelength lidar measurements: Evaluations with NASA Langley HSRL-2 during discover-AQ field campaigns, *Remote Sensing of Environment*, 222, 144-164, 2019.

Perez-Ramirez, D., Whiteman, D.N., Veselovskii, I., Korenski, M., Colarco, P., and da Silva, A.: Optimized profile retrievals of aerosol microphysical properties from simulated spaceborne multiwavelength lidar, Journal of Quantitative Spectroscopy & Radiative Transfer, 246, 106932, 2020. https://doi.org/10.1016/j.jqsrt.2020.106932

Perrone, M. R., Barnaba, F., De Tomasi, F., Gobbi, G. P., and Tafuro, A. M.: Imaginary refractive-index effects on desert-aerosol extinction versus backscatter relationships at 351 nm: numerical computations and comparison with Raman lidar measurements, Appl. Opt., 43, 5531 – 5541, 2004.

Preißler, J., Wagner, F., Guerrero-Rascado, J. L., and Silva, A. M.: Two years of free-tropospheric aerosol layers observed over Portugal by lidar, J. Geophys. Res.-Atmos., 118, 3676–3686, doi:10.1002/jgrd.50350, 2013.

Randles, C.A., Da Silva, A.M., Buchard, V., Colarco, P.R., Darmenov, A., Govindaraju, R., Smirnov, A., Holben, B., Ferrare, R., Hair, J., Shinozuka, Y., and Flynn, J.: The MERRA-2 Aerosol Reanalysis, 1980 Onward. Part I: System Description and Data Assimilation Evaluation, J. of Climate, 30, 6823-6850, 2017.

Rittmeister, F., Ansmann, A., Engelmann, R., Skupin, A., Baars, H., Kanitz, T., and Kinne, S.: Profiling of Saharan dust from the Caribbean to western Africa – Part 1: Layering structures and optical properties from shipborne polarization/Raman lidar observations, Atmos. Chem. Phys., 17, 12963–12983, https://doi.org/10.5194/acp-17-12963-2017, 2017.

Sakai, T., Nagai, T., Nakazato, M., Mano, Y., and Matsumura, T.: Ice clouds and Asian dust studied with lidar measurements of particle extinction-to-backscatter ratio, particle depolarization, and water-vapor mixing ratio over Tsukuba, Appl. Optics, 42, 7103–7116, 2003.

Shin, S.-K., Tesche, M., Kim, K., Kezoudi, M., Tatarov, B., Müller. D., and Noh, Y.: On the spectral depolarization and lidar ratio of mineral dust provided in the AERONET version 3 inversion product, Atm. Chem. Phys., 18, 12735–12746, 2018.

Sokolik, I. N., and Toon, O.B.: Incorporation of mineralogical composition into models of the radiative properties of mineral aerosol from UV to IR wavelengths, J. Geophys. Res. 104, D8, 9423 – 9444, 1999.

Soupiona, O., Papayannis, A., Kokkalis, P., Mylonaki, M., Tsaknakis, G., Argyrouli, A., and Vratolis, S.: Long-term systematic profiling of dust aerosol optical properties using the EOLE NTUA lidar system over Athens, Greece (2000-2016), *Atmospheric Environment*, **183**, 165-184, 2018.

Soupiona, O., Samaras, S., Ortiz-Amezcua, P., Böckmann, C., Papayannis, A., Moreira, G. A., Benavent-Oltra, J. A., Guerrero-Rascado, J. L., Bedoya-Velásquez, A. E., Olmo, F. J., Román, R., Kokkalis, P., Mylonaki, M., Alados-Arboledas, L., Papanikolaou, C. A., Foskinis, R.: Retrieval of optical and microphysical properties of transported Saharan dust over Athens and Granada based on multi-wavelength Raman lidar measurements: Study of the mixing processes, *Atmospheric Environment*, 214, doi.org/10.1016/j.atmosenv.2019.116824, 116824, 2019

Sun, H., Biedermann, L., and Bond, T. C.: Color of brown carbon: A model for ultraviolet and visible light absorption by organic carbon aerosol, Geophys. Res. Lett., 34, L17813, https://doi.org/10.1029/2007GL029797, 2007.

Tesche, M., Ansmann, A., Müller, D., Althausen, D., Mattis, I., Heese, B., Freudenthaler, V., Wiegner, M., Eseelborn, M., Pisani, G., and Knippertz, P.: Vertical profiling of Saharan dust with Raman lidars and airborne HSRL in southern Morocco during SAMUM, Tellus B, 61, 144–164, 2009.

Tesche, M., Groß, S., Ansmann, A., Müller, D., Althausen, D., Freudenthaler, V., and Esselborn, M.: Profiling of Saharan dust and biomass-burning smoke with multiwavelength polarization Raman lidar at Cape Verde, Tellus B, 63, 649–676, doi:10.1111/j.1600-0889.2011.00548.x, 2011.

Torres, O., Tanskanen, A., Veihelmann, B., Ahn, C., Braak, R., Bhartia, P.K., Veefkind, P., and Levelt, P.: Aerosols and surface UV products from Ozone Monitoring Instrument

observations: An overview, J. Geophys. Res., 112, D24S47, doi:10.1029/2007JD008809, 2007.

Veselovskii I., Kolgotin, A., Griaznov, V., Müller, D., Wandinger, U., Whiteman, D.: Inversion with regularization for the retrieval of tropospheric aerosol parameters from multi-wavelength lidar sounding, Appl.Opt. 41, 3685-3699, 2002.

Veselovskii I., O. Dubovik, A. Kolgotin, T. Lapyonok, P. Di Girolamo, D. Summa, D. N. Whiteman, M. Mishchenko, and D. Tanré, 2010: Application Of Randomly Oriented Spheroids For Retrieval Of Dust Particle Parameters From Multiwavelength Lidar Measurements, J. Geophys. Res., **115**, D21203, doi:10.1029/2010JD014139, 2010.

Veselovskii, I., Whiteman, D. N., Korenskiy, M., Suvorina, A., Perez-Ramirez, D.: Use of rotational Raman measurements in multiwavelength aerosol lidar for evaluation of particle backscattering and extinction, Atmos. Meas. Tech., 8, 4111–4122, 2015.

Veselovskii, I., Goloub, P., Podvin, T., Bovchaliuk, V., Derimian, Y., Augustin, P., Fourmentin, M., Tanre, D., Korenskiy, M., Whiteman, D., Diallo, A., Ndiaye, T., Kolgotin, A., Dubovik, O.: Study of African dust with multi-wavelength Raman lidar during the "SHADOW" campaign in Senegal, Atm. Chem. Phys. 16, 7013–7028, 2016.

Veselovskii, I., P. Goloub, T. Podvin, et al.: Characterization of smoke/dust episode over West Africa: comparison of MERRA-2 modeling with multiwavelength Mie-Raman lidar observations, Atm. Meas. Tech. 11, 949–969, 2018.

Wagner, R., Ajtai, T., Kandler, K., Lieke, K., Linke, C., Müller, T., Schnaiter, M., and Vragel, M.: Complex refractive indices of Saharan dust samples at visible and near UV wavelengths: a laboratory study, Atmos. Chem. Phys., 12, 2491–2512, 2012.

Whiteman, D., Melfi, S., Ferrare, R.: Raman lidar system for measurement of water vapor and aerosols in the Earth's atmosphere", Appl. Opt. 31, 3068-3082, 1992.

Xie, C., Nishizawa, T., Sugimoto, N., Matsui, I., and Wang, Z.: Characteristics of aerosol optical properties in pollution and Asian dust episodes over Beijing, China, Appl. Opt., 47, 4945 – 4951, 2008.

Captures to figures

Fig.1. The aerosol optical depth (AOD) at 532 nm (open circles) and AODs of the main aerosol components, such as dust, organic carbon (OC), black carbon (BC), sulfates (SU) and sea salt (SS) provided by the MERRA-2 for (a) March, (b) April and (c) December 2015 over Mbour. Open stars show AOD_{532} provided by AERONET.

Fig.2. Aerosol single scattering albedo (SSA) at 675 nm and 440 nm provided by AERONET for M'bour site in 2015.

Fig.3. Tempo-spatial distributions of aerosol backscattering coefficient β_{532} (left column), particle depolarization ratio δ_{532} (middle column) and water vapor mixing ratio (right column) for the nights 1-2 April (upper row), 2-3 April (middle row) and 3-4 April 2015 (bottom row).

Fig.4. Three-day backward trajectories for the air mass in M'bour on 2, 3, 4 April 2015 at 03:00 UTC obtained with the HYSPLIT model.

Fig.5. Vertical profiles of extinction coefficients (α_{355}, α_{532}) and lidar ratios (S_{355}, S_{532}) at 355 nm and 532 nm together with particle depolarization ratio δ_{532} measured on 1 April (20:40-22:20 UTC), 2-3 April (23:40-04:30 UTC) and 3-4 April 2015 (23:00-02:00 UTC). Symbols show the lidar ratios of dust provided by MERRA-2 model ($S_{355}M$, $S_{532}M$).

Fig.6. Backscattering coefficients for observations presented in Fig.5 for 2-3 and 3-4 April.

Fig.7. Vertical profiles of the extinction and backscattering Ångström exponents (A_α and A_β) at 355 – 532 nm for three temporal intervals from Fig.5.

Fig.8. Vertical profiles of (a) extinction coefficients at 355 nm and 532 nm (α_{355}, α_{532}) measured by lidar (lines) and modeled by MERRA-2 (line+symbol) for five aerosol components at 532 nm; (b) extinction Ångström exponents at 355-532 nm obtained from lidar observations and modeled by MERRA-2 for pure dust (stars) together with water vapor mixing ratio (WVMR) and the relative humidity; (c) contribution of dust and smoke particles to β_{532} together with particle depolarization ratio δ_{532}. Values of WVMR are multiplied by factor 10. Lidar measurements were performed on 3-4 April 2015 for period 23:00 – 02:00 UTC. Modeling results are given for 4 April 00:00 UTC.

Fig.9. (a, c) Vertical profiles of extinction coefficients (α_{355}, α_{532}) and lidar ratios (S_{355}, S_{532}) at 355 nm and 532 nm; together with (b, d) particle depolarization ratio δ_{532}, and extinction and backscattering Ångström exponents (A_α, A_β) measured on (a, b) 14 April 2015 (00:00 – 05:00 UTC) and (c, d) the night 23-24 April (23:00-06:00 UTC). Open symbols on plots (a, c) show the lidar ratios $S_{355}M$ and $S_{532}M$ provided by MERRA-2 model on 14 and 14 April at 00:00 UTC.

Fig.10. Four-days backward trajectories for 14 April (03:00 UTC) and 24 April (00:00 UTC) 2015 obtained with the HYSPLIT model.

Fig.11. Lidar ratios S_{355}, S_{532} and the particle depolarization ratio δ_{532} for dust episodes in March - April 2015. Open triangles show the ratio S_{355}/S_{532}.

Fig.12. Imaginary part of the refractive index at 440 nm and 675 nm provided by AERONET in March – April 2015

Fig.13. Difference Im_{440} - Im_{675} from Fig.12 together with lidar measured values S_{355}/S_{532} from Fig.11 for days in April 2015

Fig.14. The particle size distributions provided by AERONET on 2 and 23 April 2015 (three PSDs for each day). Red line shows the PSD derived from 3β+2α lidar measurements on 23-24 April within 2.0 – 3.0 km height range.

Fig.15. Lidar ratios S_{355}, S_{532} together with the extinction and backscattering Ångström exponents A_α and A_β calculated for (a) AERONET PSD on 23 April from Fig.14 and (b) lidar derived PSD from Fig.14 as a function of the imaginary part. Open stars show A_β for spectrally dependent imaginary part Im(λ), assuming that Im_{532}=0.002 is fixed and only Im_{355} is free vary. Computations are performed for the assembly of randomly oriented spheroids with the real part Re=1.55.

Fig.16. Infrared Difference Dust Index (IDDI) derived from MSG geostationary satellite at noon time. Panels (a), (b) show IDDI elevated values, representing airborne dust emission and transport, over central and northern Sahara on 29, 30 March 2015. The dust transport regime is visibly changed a few days later (17, 18 April 2015, panels (c), (d)); the elevated IDDI values are shifted to the south. The areas in white are cloud screened pixels; the IDDI is derived only over land due to the algorithm physical principle.

Fig.17. Tempo-spatial distributions of aerosol backscattering coefficient β_{532}, particle depolarization ratio δ_{532} and water vapor mixing ratio during smoke episode on the night 14-15 December 2015.

Fig.18. Vertical profiles of (a) extinction coefficients (α_{355}, α_{532}) and lidar ratios (S_{355}, S_{532}); (b) extinction, backscattering Ångström exponents (A_α, A_β) at 355 – 532 nm and relative humidity RH; (c) contribution of dust and smoke to β_{532} together with particle depolarization ratio δ_{532} on 15 December (04:00 – 06:00 UTC). Black line in plot (a) shows the lidar ratio of smoke S_{532}^{s} calculated from Eq.5.

Fig.19. Modeled lidar ratios of organic carbon at 355 nm and 532 nm (line + symbol) as a function of the relative humidity for the particle parameters used in the MERRA-2 model. At 355 nm results are given for four values of the imaginary part of dry particles: Im_{355}= 0.048, 0.03. 0.02, 0.01. At 532 nm two values Im_{532}= 0.009 and 0.005 are considered. The scattered symbols (circles) show the lidar ratios (S_{355}, S_{532}) observed during five smoke episodes from Table 1.

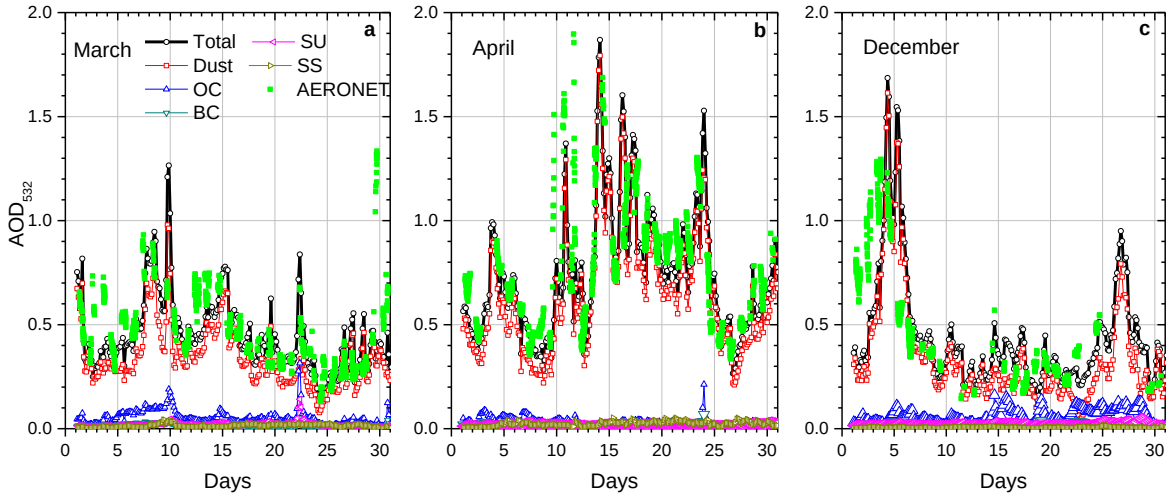

Fig.1. The aerosol optical depth (AOD) at 532 nm (open circles) and AODs of the main aerosol components, such as dust, organic carbon (OC), black carbon (BC), sulfates (SU) and sea salt (SS) provided by the MERRA-2 for (a) March, (b) April and (c) December 2015 over Mbour. Open stars show AOD_{532} provided by AERONET.

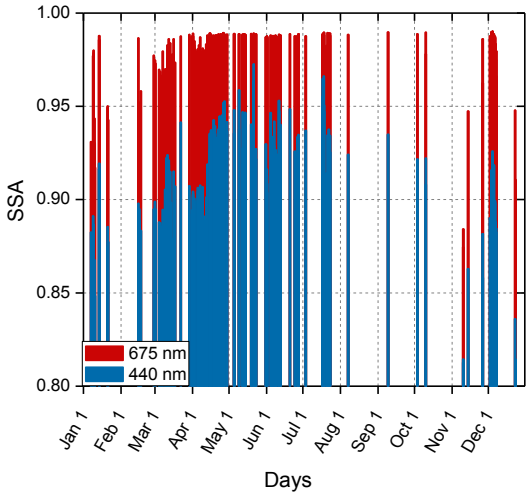

Fig.2. Aerosol single scattering albedo (SSA) at 675 nm and 440 nm provided by AERONET for M'bour site in 2015.

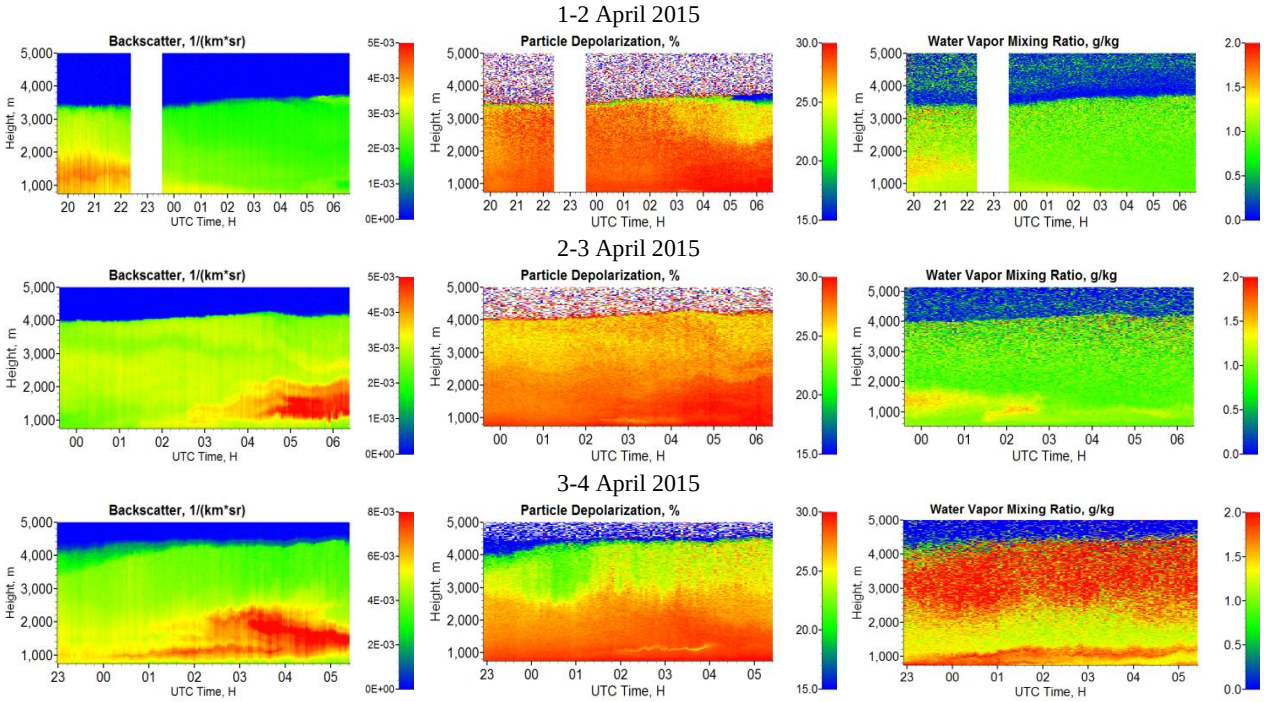

Fig.3. Tempo-spatial distributions of aerosol backscattering coefficient β_{532} (left column), particle depolarization ratio δ_{532} (middle column) and water vapor mixing ratio (right column) for the nights 1-2 April (upper row), 2-3 April (middle row) and 3-4 April 2015 (bottom row).

929
930

02 April 03:00 | 03 April 03:00 | 04 April 03:00

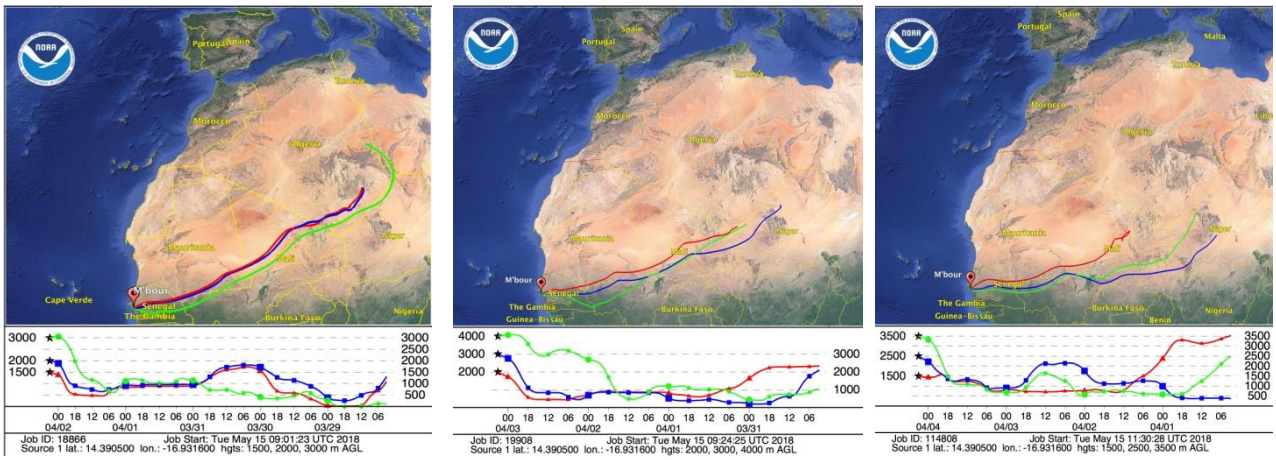

931 Fig.4. Three-day backward trajectories for the air mass in M'bour on 2, 3, 4 April 2015 at 03:00
932 UTC obtained with the HYSPLIT model.
933

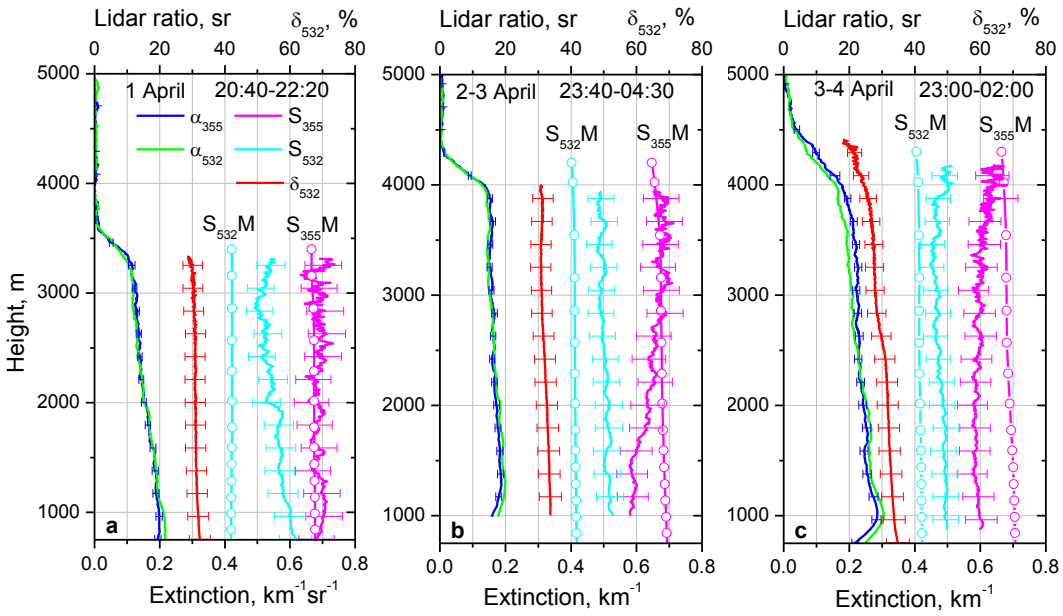

934 Fig.5. Vertical profiles of extinction coefficients (α_{355}, α_{532}) and lidar ratios (S_{355}, S_{532}) at 355 nm
935 and 532 nm together with particle depolarization ratio δ_{532} measured on 1 April (20:40-22:20
936 UTC), 2-3 April (23:40-04:30 UTC) and 3-4 April 2015 (23:00-02:00 UTC). Symbols show the
937 lidar ratios of dust provided by MERRA-2 model ($S_{355}M$, $S_{532}M$).

938

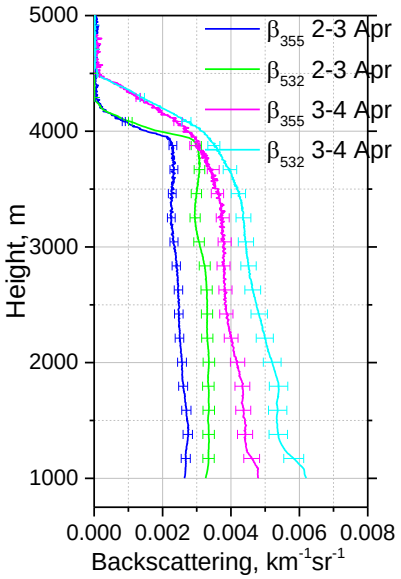

939

940 Fig.6. Backscattering coefficients for observations presented in Fig.5 for 2-3 and 3-4 April.

941

942

943

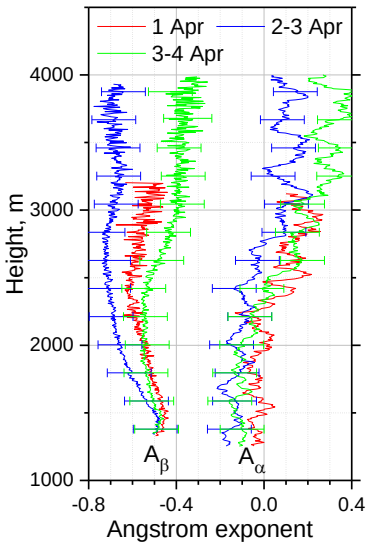

944

945 Fig.7. Vertical profiles of the extinction and backscattering Ångström exponents (A_α and A_β) at
946 355 – 532 nm for three temporal intervals from Fig.5.

947

948

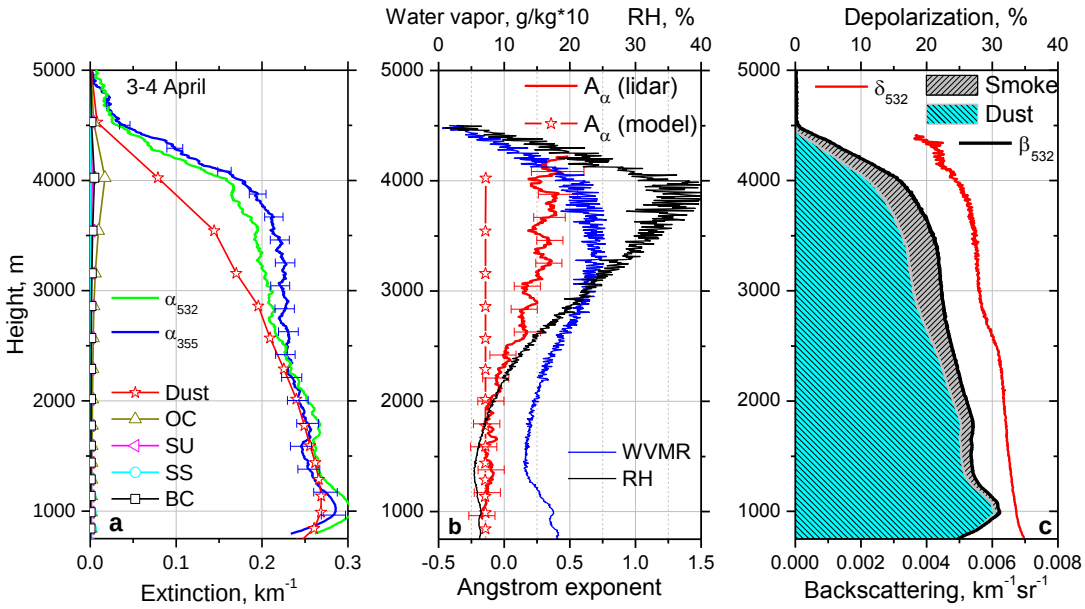

Fig.8. Vertical profiles of (a) extinction coefficients at 355 nm and 532 nm (α_{355}, α_{532}) measured by lidar (lines) and modeled by MERRA-2 (line+symbol) for five aerosol components at 532 nm; (b) extinction Ångström exponents at 355-532 nm obtained from lidar observations and modeled by MERRA-2 for pure dust (stars) together with water vapor mixing ratio (WVMR) and the relative humidity; (c) contribution of dust and smoke particles to β_{532} together with particle depolarization ratio δ_{532}. Values of WVMR are multiplied by factor 10. Lidar measurements were performed on 3-4 April 2015 for period 23:00 – 02:00 UTC. Modeling results are given for 4 April 00:00 UTC.

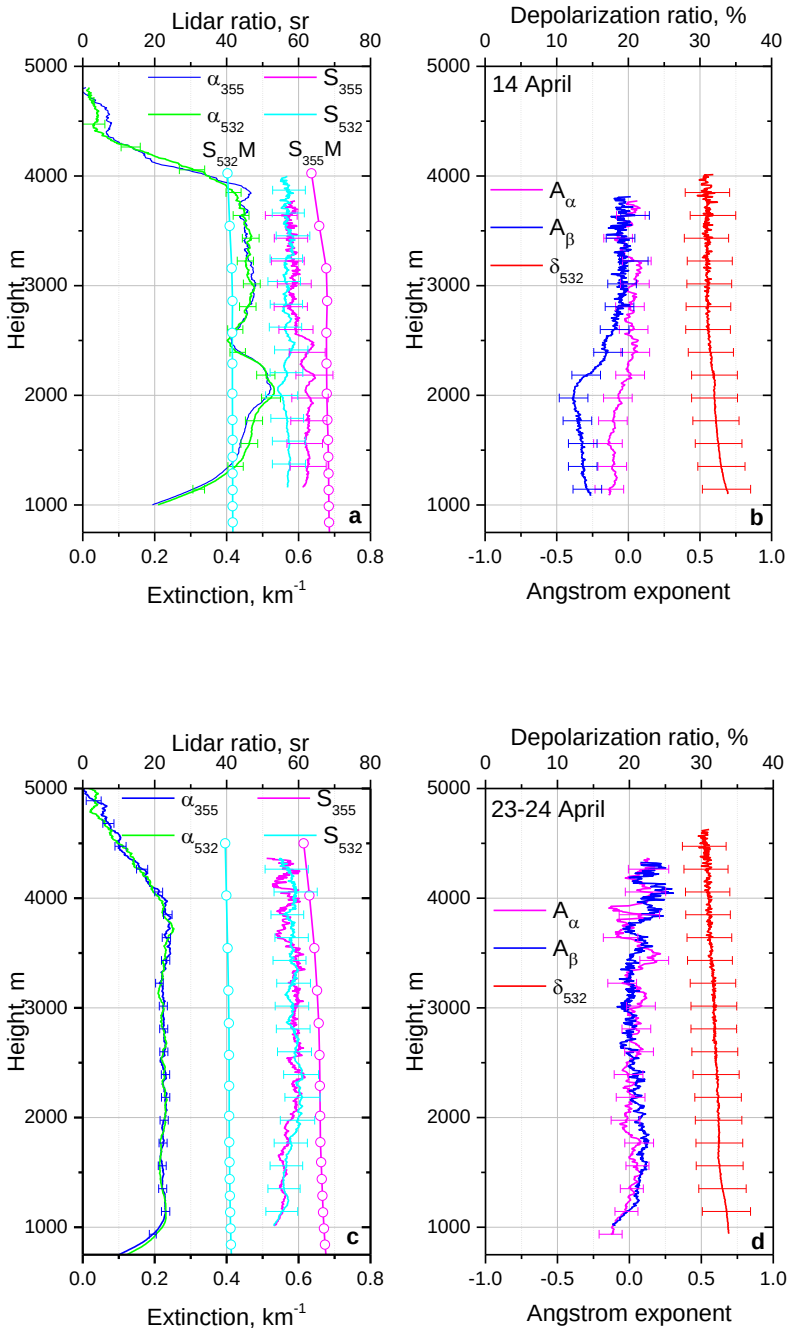

Fig.9. (a, c) Vertical profiles of extinction coefficients (α_{355}, α_{532}) and lidar ratios (S_{355}, S_{532}) at 355 nm and 532 nm; together with (b, d) particle depolarization ratio δ_{532}, and extinction and backscattering Ångström exponents (A_α, A_β) measured on (a, b) 14 April 2015 (00:00 – 05:00 UTC) and (c, d) the night 23-24 April (23:00-06:00 UTC). Open symbols on plots (a, c) show the lidar ratios $S_{355}M$ and $S_{532}M$ provided by MERRA-2 model on 14 and 14 April at 00:00 UTC.

14 April	24 April
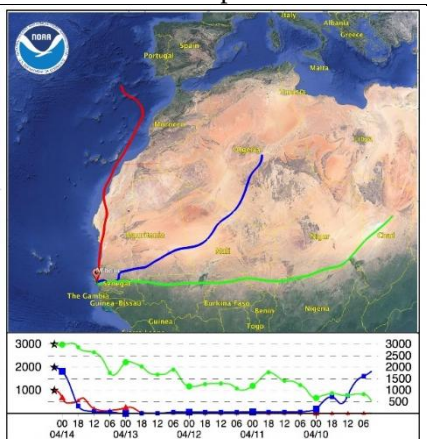	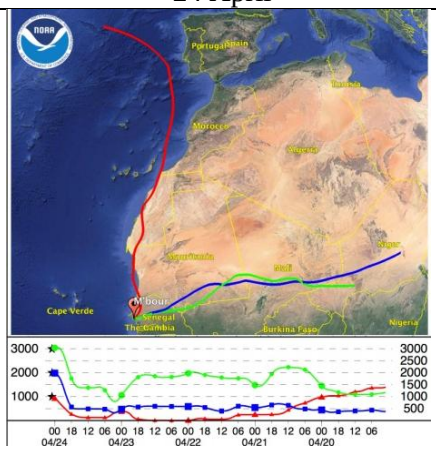

Fig.10. Four-days backward trajectories for 14 April (03:00 UTC) and 24 April (00:00 UTC) 2015 obtained with the HYSPLIT model.

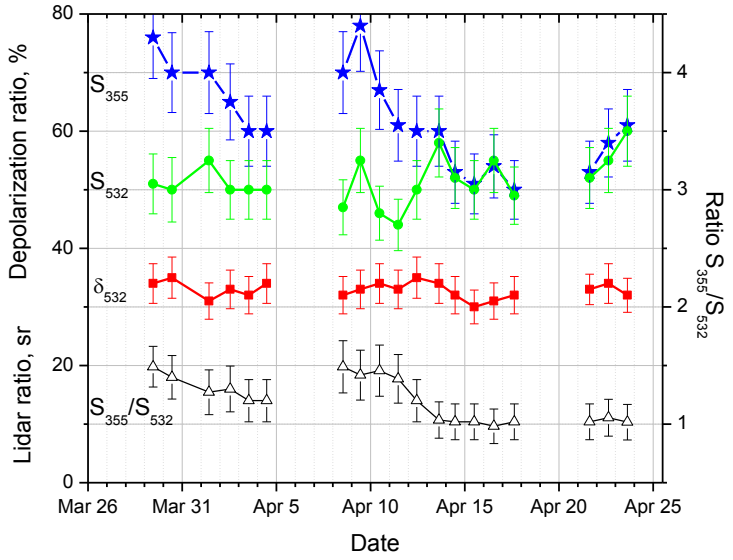

Fig.11. Lidar ratios S_{355}, S_{532} and the particle depolarization ratio δ_{532} for dust episodes in March - April 2015. Open triangles show the ratio S_{355}/S_{532}.

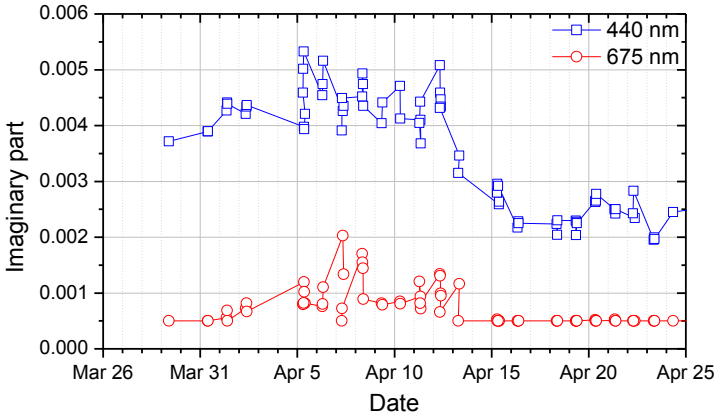

Fig.12. Imaginary part of the refractive index at 440 nm and 675 nm provided by AERONET in March – April 2015

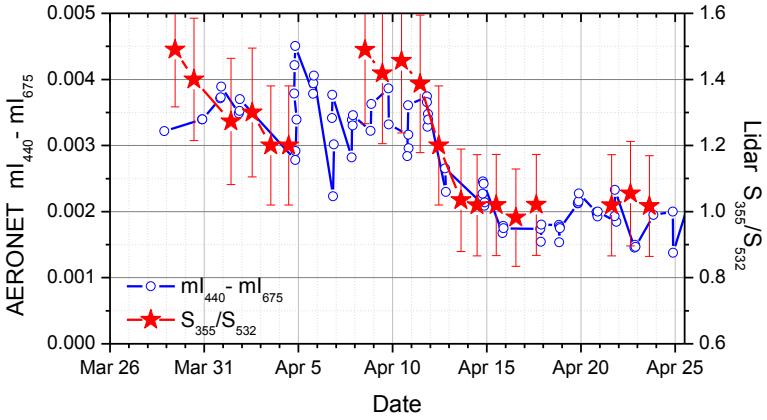

Fig.13. Difference Im_{440} - Im_{675} from Fig.12 together with lidar measured values S_{355}/S_{532} from Fig.11 for days in April 2015.

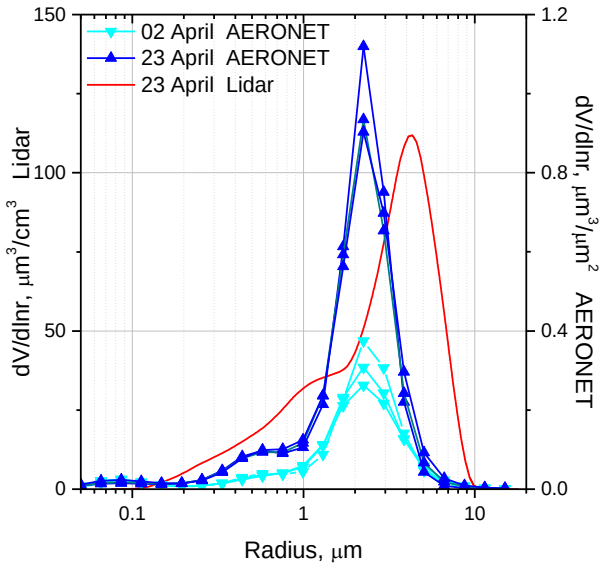

Fig.14. The particle size distributions provided by AERONET on 2 and 23 April 2015 (three PSDs for each day). Red line shows the PSD derived from 3β+2α lidar measurements on 23-24 April within 2.0 – 3.0 km height range.

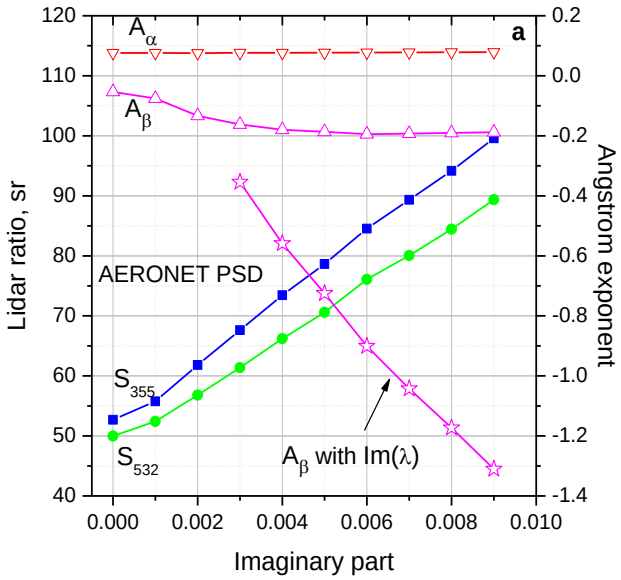

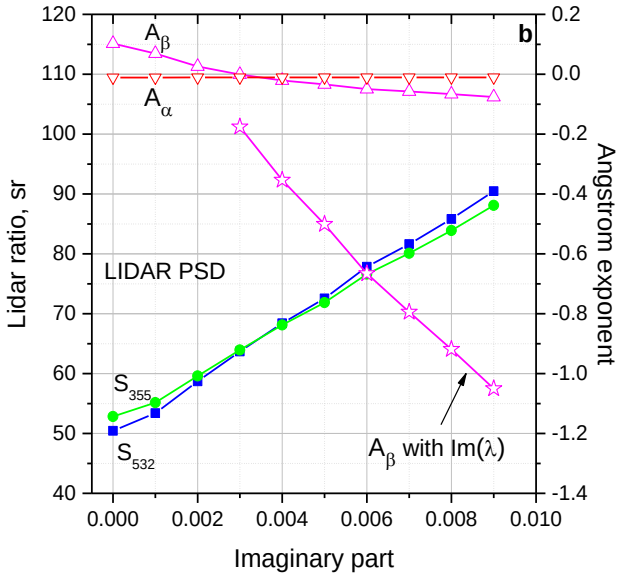

Fig.15. Lidar ratios S_{355}, S_{532} together with the extinction and backscattering Ångström exponents A_α and A_β calculated for (a) AERONET PSD on 23 April from Fig.14 and (b) lidar derived PSD from Fig.14 as a function of the imaginary part. Open stars show A_β for spectrally dependent imaginary part Im(λ), assuming that Im_{532}=0.002 is fixed and only Im_{355} is free vary. Computations are performed for the assembly of randomly oriented spheroids with the real part Re=1.55.

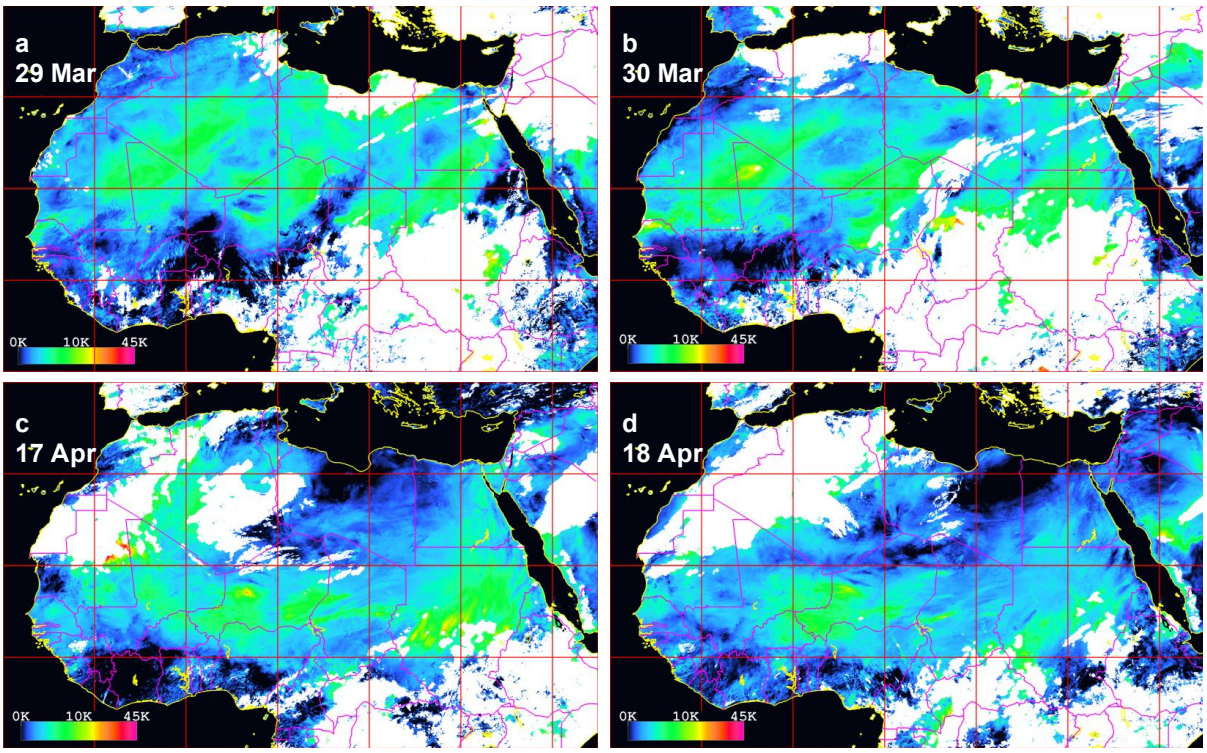

Fig.16. Infrared Difference Dust Index (IDDI) derived from MSG geostationary satellite at noon time. Panels (a), (b) show IDDI elevated values, representing airborne dust emission and transport, over central and northern Sahara on 29, 30 March 2015. The dust transport regime is visibly changed a few days later (17, 18 April 2015, panels (c), (d)); the elevated IDDI values are shifted to the south. The areas in white are cloud screened pixels; the IDDI is derived only over land due to the algorithm physical principle.

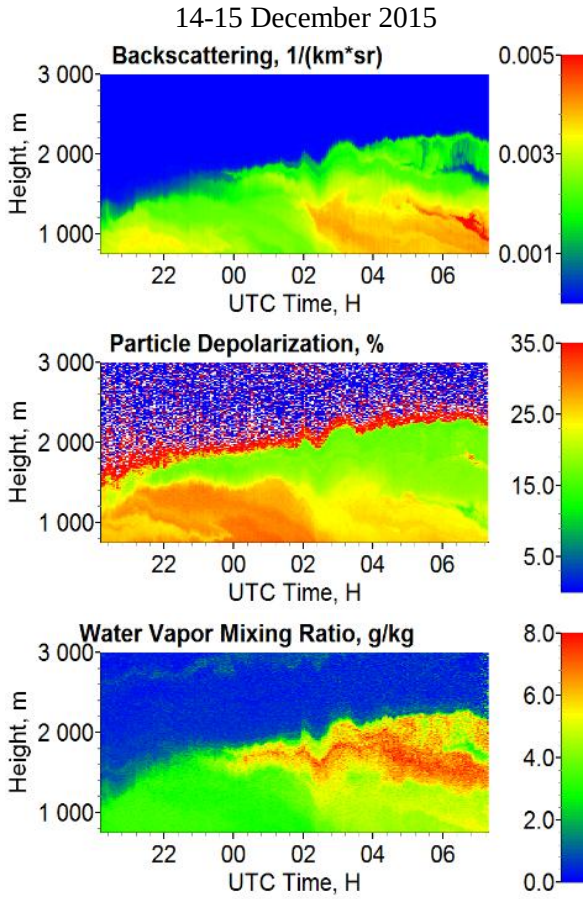

Fig.17. Tempo-spatial distributions of aerosol backscattering coefficient β_{532}, particle depolarization ratio δ_{532} and water vapor mixing ratio during smoke episode on the night 14-15 December 2015.

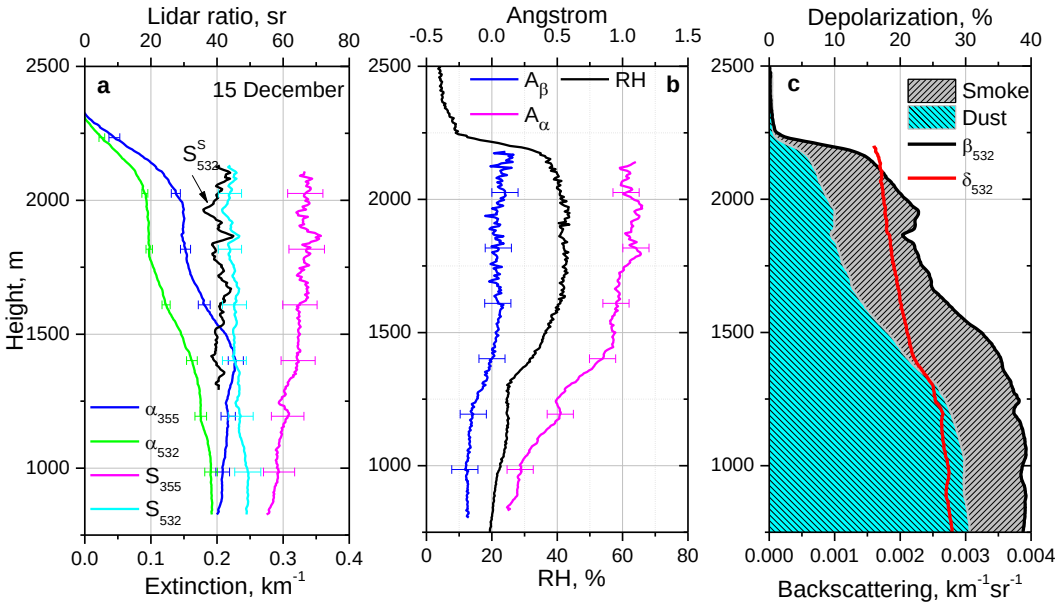

Fig.18. Vertical profiles of (a) extinction coefficients (α_{355}, α_{532}) and lidar ratios (S_{355}, S_{532}); (b) extinction, backscattering Ångström exponents (A_α, A_β) at 355 – 532 nm and relative humidity RH; (c) contribution of dust and smoke to β_{532} together with particle depolarization ratio δ_{532} on 15 December (04:00 – 06:00 UTC). Black line in plot (a) shows the lidar ratio of smoke S^s_{532} calculated from Eq.5.

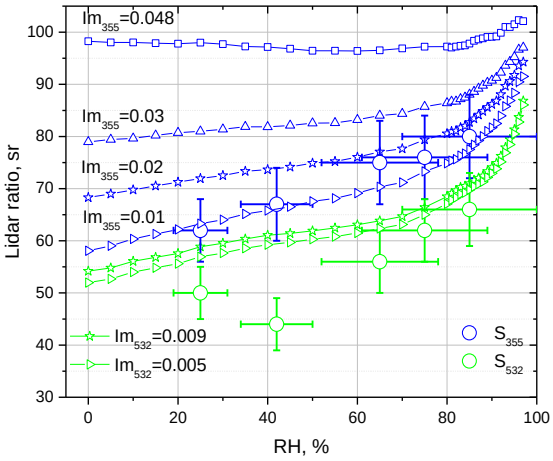

Fig.19. Modeled lidar ratios of organic carbon at 355 nm and 532 nm (line + symbol) as a function of the relative humidity for the particle parameters used in the MERRA-2 model. At 355 nm results are given for four values of the imaginary part of dry particles: Im_{355}= 0.048, 0.03. 0.02, 0.01. At 532 nm two values Im_{532}= 0.009 and 0.005 are considered. The scattered symbols (circles) show the lidar ratios (S_{355}, S_{532}) observed during five smoke episodes from Table 1.